Beyond zircon fingerprinting: Zircon and TiO2 polymorphs constrain genealogy and evolution of the New Caledonian ophiolite

Daniel Patias, Renjie Zhou, Jonathan Aitchison, Dominique Cluzel, Trevor Ireland, Dongyang Lian, Jingsui Yang

▶ **To cite this version:**

Daniel Patias, Renjie Zhou, Jonathan Aitchison, Dominique Cluzel, Trevor Ireland, et al.. Beyond zircon fingerprinting: Zircon and TiO2 polymorphs constrain genealogy and evolution of the New Caledonian ophiolite. Chemical Geology, 2024, 644, pp.121841. 10.1016/j.chemgeo.2023.121841 . hal-04362970

HAL Id: hal-04362970

https://cnrs.hal.science/hal-04362970v1

Submitted on 23 Dec 2023

HAL is a multi-disciplinary open access archive for the deposit and dissemination of scientific research documents, whether they are published or not. The documents may come from teaching and research institutions in France or abroad, or from public or private research centers.

L'archive ouverte pluridisciplinaire **HAL**, est destinée au dépôt et à la diffusion de documents scientifiques de niveau recherche, publiés ou non, émanant des établissements d'enseignement et de recherche français ou étrangers, des laboratoires publics ou privés.

Manuscript

Click here to access/download;Manuscript;01_Patias_NC zircon and TiO2 polymorphs_2.docx

Click here to view linked References

Beyond zircon fingerprinting: Zircon and TiO_2 polymorphs constrain genealogy and evolution of the New Caledonian ophiolite

Daniel Patias[a]*, Renjie Zhou[a], Jonathan C. Aitchison[a], Dominique Cluzel[b], Trevor Ireland[a], Dongyang Lian[c], Jingsui Yang[d]

[a] School of the Environment, The University of Queensland, St Lucia, QLD 4072, Australia

[b] Institute of Pure and Applied Sciences, Université de la Nouvelle-Calédonie, BP R4, 98851 Nouméa, New Caledonia

[c] School of Earth Sciences and Engineering, Nanjing University, Nanjing 210023, China

[d] Institute of Geology, Chinese Academy of Geological Sciences (CAGS), Beijing 100037, China

* Correnponding author: d.patias@uq.edu.au

Abstract

Ophiolitic ultramafic rocks play a crucial role in understanding deep geochemical cycling and the transfer of components associated with slab-mantle interactions. Detailed geochronological and geochemical analysis of zircon and TiO_2 polymorphs present within mantle rocks of the Eocene New Caledonian ophiolite reveal discrete magmatic and xenocrysts populations amongst harzburgite from Me Maoya and chromitite from Tiébaghi. Most of the mineral grains examined in this study have a xenocrystic origin and are concentrated particularly in the harzburgite. They are inferred to have been recycled from the northern end of the Norfolk Ridge that formed the leading edge of a thin continental slab of Gondwana affinity which had previously rifted from eastern Australia together with other elements of Zealandia. The slab was drawn into an intra-oceanic subduction zone beneath the proto-Loyalty arc immediately prior to emplacement of the forearc ophiolite today represented by the New Caledonian Peridotite Nappe. The pristine isotopic systems preserved in the studied minerals indicate they were recycled into the mantle wedge at moderate mantle depths (above 60 – 80 km depth) within in the subduction channel. In contrast, Eocene U-Pb ages of zircon and rutile grains that mostly occur within in the Tiebaghi chromitite indicate formation through magmatic processes, likely associated with late-stage percolation of enriched fluids and melt. Overlapping ages of the Eocene zircon and rutile grains, Ar-Ar pargasite ages, and ages of cross-cutting dikes in the Tiébaghi chromitite provide evidence that it cooled at ca. 47-46 Ma. This study demonstrates the capacity to enhance our comprehension of forearc mantle wedge evolution by examining geochronological and thermochronometer minerals within ultramafic rocks. It also highlights the potential for studying recycled solid mineral phases, tracing their thermal evolution, and characterizing potential subducted source terranes.

Keywords: Forearc mantle-wedge; Slab-mantle interaction; subduction processes; Ultramafic rocks; U-Pb dating; trace element geochemistry

1. Introduction

Subduction zones are the loci of fundamental Earth processes associated with the deep geochemical cycle and the transfer of components from subducting lithospheric slabs to overriding shallower levels in the forearc mantle (Pearce et al., 1984; Dilek and Furnes, 2011; Agard et al., 2020). These processes involve the recycling of solid, fluid, and gaseous components, and are moderated by geological parameters such as the age and temperature of the subducting slab and/or thickness of its sedimentary cover (e.g., Yu et al., 2020; Aitchison et al., 2022). Investigation of supra-subduction ophiolitic mantle-rocks, that develop in the forearc mantle wedge (Pearce et al., 1984), provides a key approach to fingerprinting processes associated with subduction zones and slab-mantle interaction (Soret et al., 2016; Yu et al., 2020). In recent decades, there have been significant advances in the understanding of forearc systems and ophiolites (Reagan et al., 2010; Dilek and Furnes, 2011). However, crucial knowledge gaps remain, such as the extent and effects of recycling of components and the timescale of processes related to mantle wedge evolution. To a certain degree, uncertainties reflect the rarity of preserved ophiolitic ultramafic sections, as they represent the most prominent feature to investigate the slab-mantle interaction. Furthermore, the refractory nature and highly altered state of these materials due to serpentinization and metasomatism make their investigation challenging.

Until now geochronological data for ophiolitic rocks, such as zircon U-Pb or amphibole Ar-Ar age determinations have been widely applied to understanding crustal sections or the timing of formation of high-grade metamorphic sole rocks but less so to mantle lithologies. Remarkably in recent decades, and somewhat unexpectedly given their refractory nature, the discovery of zircons and other datable minerals in depleted ophiolitic mantle rocks has become more common (Yamamoto et al., 2013; Aitchison et al., 2022; Cluzel et al., 2022). Their occurrence can contribute to a better understanding of the evolution of the forearc mantle wedge and associated processes.

Among minerals recovered from ultramafic ophiolitic rocks worldwide, those datable using U-Pb geochronology include both zircon and rutile. Commonly these minerals display a range of ages that predate the ophiolite formation suggesting they are xenocrystic (Aitchison et al., 2022; Cluzel et al., 2022). However, in addition to these inherited crystals, zircons and rutiles ages that are contemporaneous with the hosting ophiolite have also been reported (González-Jiménez et al., 2017; Pujol-Solà et al., 2020; Cluzel et al., 2022).

Previous studies have typically used geochronological data to fingerprint the timing of ophiolite genesis and obduction. However, as analytical capabilities increase, it is possible to

glean additional geochemical and isotopic data that specifically characterise individual mineral species' sources and thermal evolution. Moreover, differences amongst distinct age populations of the same mineral can also be characterised and investigated, including geochronometers locked in at different pressures. Thus, we can now move beyond fingerprinting to understanding the genealogy and evolution of the mineral constituents of an ophiolite and raise understanding to a new level.

This study presents extensive mineralogical, geochronological, and geochemical datasets for zircon and two TiO_2 polymorphs, rutile and anatase, extracted from harzburgite and podiform chromitite of the Peridotite Nappe in New Caledonia. These minerals exhibit distinct colors and morphologies. They display a wide range of geochemical signatures and U-Pb ages, providing a comprehensive dataset for understanding the geological history of the region. Notably, xenocrysts demonstrate a robust affinity to terranes that were subducting beneath a developing intra-oceanic island arc system. The occurrence and isotopic system of these xenocrysts provide important information about the depth at which recycling processes took place within the forearc wedge. Furthermore, the U-Pb zircon and rutile ages, contemporaneous with the formation of the Peridotite Nappe, reveal unique chemical and isotopic signatures that contribute crucial insights into the processes involved in the ophiolite's evolution.

2. Regional context

New Caledonia in the SW Pacific, forms a part of the Norfolk Ridge, the present configuration of which is attributed to the rift and drift processes that occurred during the Mesozoic Period, along the Eastern Gondwana margin (Cluzel et al., 2012b; Collot et al., 2020). The main island, Grande Terre, covers an area of 400 length and 50 km width, and comprises a diverse range of Permian to Eocene rocks, encompassing igneous, sedimentary, and metamorphic terranes (Paris, 1981; Aitchison et al., 1995). Across Grande Terre, large massifs of peridotite and mafic plutonic rocks known as the Peridotite Nappe or New Caledonia Ophiolite comprise one of the largest exposures of ultramafic bodies on Earth (Avias, 1967; Collot et al., 1987) (Fig. 1). This nappe is interpreted as a fragment of forearc mantle and lower crust associated with the proto-Loyalty arc (Cluzel et al., 2012b). During Eocene arc-continent collision, it was obducted to the SW over the Gondwana margin continental fragment, which had earlier rifted off eastern Australia as part of Zealandia (Collot et al., 1987; Aitchison et al., 1995; Cluzel et al., 2001, 2016; Mortimer et al., 2017).

The ophiolitic rocks are generally undeformed and exhibit a basal contact zone containing a brecciated serpentinite sole above a tectonic contact with a footwall of oceanic crustal rocks of the Late Cretaceous-Paleocene Poya terrane (A.Fig. 1) (Collot et al., 1987; Cluzel et al., 2018; Maurizot et al., 2020b). The nappe is primarily composed of harzburgites with lenses of dunites, lherzolites, and chromitites. Locally, mafic-ultramafic cumulates such as dunite, wehrlite, pyroxenite, and gabbro also occur (Pirard et al., 2013; Secchiari et al., 2016). Typical upper crustal rocks commonly found in other ophiolites, such as pillow basalts and sheeted dykes are notably absent from the Peridotite Nappe (Avias, 1967).

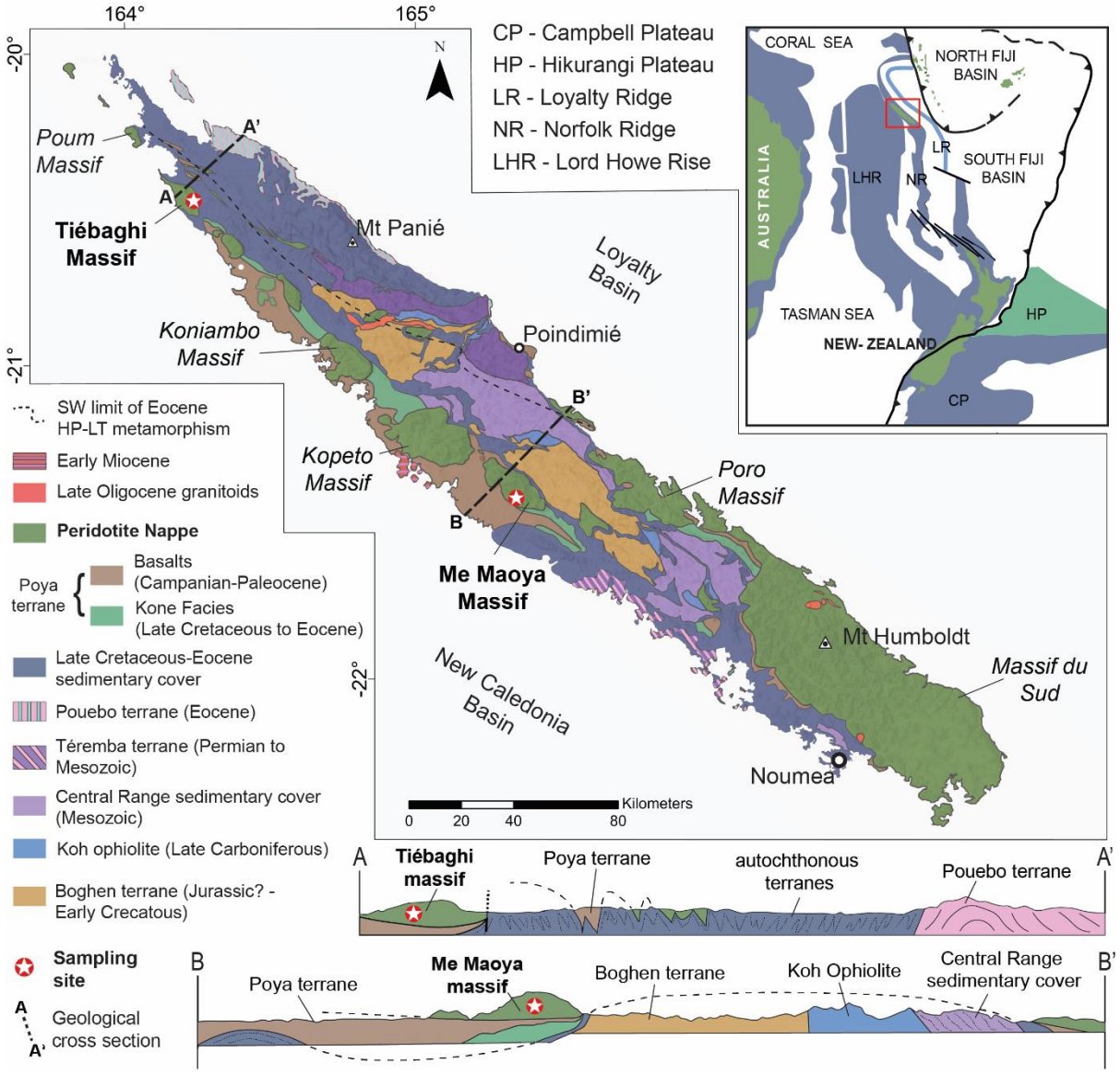

Figure 1. Geological map of New Caledonia exhibiting the main tectonic units and sample locations (Adapted after Aitchison et al., 2022). Cross sections adapted after Maurizot et al. (2020b).

123 The Peridotite Nappe is known for its diverse geochemical, isotopic, and petrological
124 characteristics, resulting from multi-stage magmatic evolution including melt extraction,
125 melt-rock interaction, and refertilization (Ulrich et al., 2010; Pirard et al., 2013; Secchiari et
126 al., 2016). Lherzolites in the northern massifs of Tiébaghi and Poum have REE patterns
127 resembling abyssal peridotites (Ulrich et al., 2010; Secchiari et al., 2016), while harzburgites,
128 which dominate the nappe are marked by low REE content and U-shaped REE patterns
129 similar to modern forearc ophiolites, reflecting high degrees of partial melting (Pirard et al.,
130 2013; Secchiari et al., 2016). They are also characterized by high Fo olivine (89.5-92.9
131 mol%), high Mg# orthopyroxene (89.8-94.2), Cr-rich spinel (Cr# 44-72), and a lack of
132 primary clinopyroxene (Ulrich et al., 2010; Pirard et al., 2013; Secchiari et al., 2020b).
133 Petrographic elements, such as secondary ortho- and clinopyroxene, are interpreted to have
134 formed in association with later refertilization in a supra-subduction environment (Ulrich et
135 al., 2010). Whole-rock isotopic data, with εNd_i ranging from -0.80 to +13.32 and $^{87}Sr/^{86}Sr$
136 from 0.70257 to 0.70770, also suggest a subduction-related influx associated with the melting
137 of sedimentary rocks (Secchiari et al., 2020b). The presence of dikes with adakite-like,
138 island-arc tholeiites (IAT), and boninitic geochemical signatures cutting through the mantle
139 section further supports this interpretation (Maurizot et al., 2020b). Together these features
140 make the Peridotite Nappe a valuable unit for studying the formation and development of
141 forearc mantle rocks (e.g., Parrot and Dugas, 1980; Aitchison et al., 1995; Ulrich et al., 2010;
142 Liu et al., 2018).

143 Geochronological data for the Peridotite Nappe provide information crucial to
144 understanding its formation, cooling, and Paleogene obduction. U/Pb zircon and Ar/Ar
145 amphibole ages indicate that granulite-facies mafic rocks formed circa 56 Ma in a
146 metamorphic sole, which is potentially linked to subduction initiation processes (Cluzel et al.,
147 2012a; Soret et al., 2016). The main magmatic episode in the forearc is estimated to have
148 occurred around 53.1 ± 0.4 Ma (n=19) based on zircon U/Pb ages from dikes with a supra-
149 subduction geochemical affinity that intrude the mantle sequence (Cluzel et al., 2006;
150 Maurizot et al., 2020b). Cooling is estimated to have occurred between 50 and 47 Ma, as
151 inferred from Ar/Ar ages obtained on boninitic glass (Cluzel et al., 2016). Obduction over
152 basement rocks associated with the northern extent of the Norfolk Ridge (part of Zealandia)
153 took place during in the late Eocene circa 37-34 Ma, according to thermochronological (Ar-
154 Ar K-feldspar and apatite fission track data; Baldwin et al., 1999) and micropaleontological
155 dating (Maurizot et al., 2020a). This marks the last significant tectonic event related to this
156 ophiolite.

3. Samples

Two samples of approximately 500 kg of harzburgite and chromitite were collected from the Me Maoya and Tiébaghi massifs, respectively, to examine for the rare presence of zircon and rutile in ultramafic rocks. Unaltered harzburgite boulders were collected from the bed of the Baraoua River in the Me Moya massif (sample coordinates: 21°27'58.96"S; 165°23'40.11" E). Chromitites were obtained from stockpiles at the Tiébaghi massif chrome mine wash-plant (GPS 20°26'15.49" S; 164°13'46.02" E) ore mined from circa 300 m below surface levels.

Harzburgite from the Me Maoya massif (Fig. 2a) is exceptionally fresh and composed of olivine, orthopyroxene, and chromium-rich spinel (Fig. 2b), with clinopyroxene appearing as a late-stage exsolution phase. This spinel-harzburgite is primarily formed of high-temperature mineral assemblages (Pirard et al., 2013), as suggested by various geothermometers. Ca-in-orthopyroxene estimates temperatures of approximately 1020°C (range: 903-1185°C), while the Ca-in-olivine (average $T_{Ol\text{-}in\text{-}Ca}$ = 842°C) and olivine-spinel (average $T_{Ol\text{-}Sp}$ = 924°C) geothermometers suggest slightly cooler conditions (Secchiari et al., 2020b, 2022). Based on olivine-spinel oxy-barometers ranging from 0.35 to 0.92 (Secchiari et al., 2020a) the harzburgites generally exhibit oxygen fugacity values (ΔFMQ), similar to peridotites from the Izu-Bonin forearc (Parkinson and Pearce, 1998), consistent with a likely subduction-related origin.

At the now inoperative Tiébaghi chrome mine, one of the largest and richest chrome deposits on Earth, irregular pods of chromitite occur enveloped by dunite and surrounded by diopside harzburgite on top and harzburgite at the base (Moutte, 1982). Chromitite pods dip steeply (60-70° SW) parallel to the high-temperature foliation amongst the surrounding peridotite (Cassard et al., 1981). They comprise primary Cr-rich spinel (Cr_2O_3 wt % >40%), olivine and orthopyroxene with serpentinization occurring as a later phase. The collected sample is a massive chromitite (Fig. 2c), with olivine and orthopyroxene as minor phases, and serpentine filled cracks between chromite grains. Rocks from the Tiébaghi massif also exhibit chromitite with distinct textures, which include small nodular chromitite interlayered with dunite that is cross-cut by hydrous silicate venules (Fig. 2d), pargasite dominant sample encompassing Cr-spinel crystals (Fig. 2e), and Cr-rich rock cut by small nodular chromitite veins crosscut by hydrous silicate venules (Fig. 2f). These different textural relationships indicate that several phases of melts and fluids were involved in the formation of Tiébaghi massif, commonly revealing the presence of hydrous silicates (e.g., pargasite, Na-rich phlogopite, and tremolite), previously described by Moutte (1982) and dated at ca. 47 Ma

($^{40}Ar/^{39}Ar$ in pargasite; Cluzel et al., 2022). In addition, boulders of mafic and intermediate magmatic rocks can be observed in the stockpile and throughout the massif suggesting that more evolved melts likely percolated the massif.

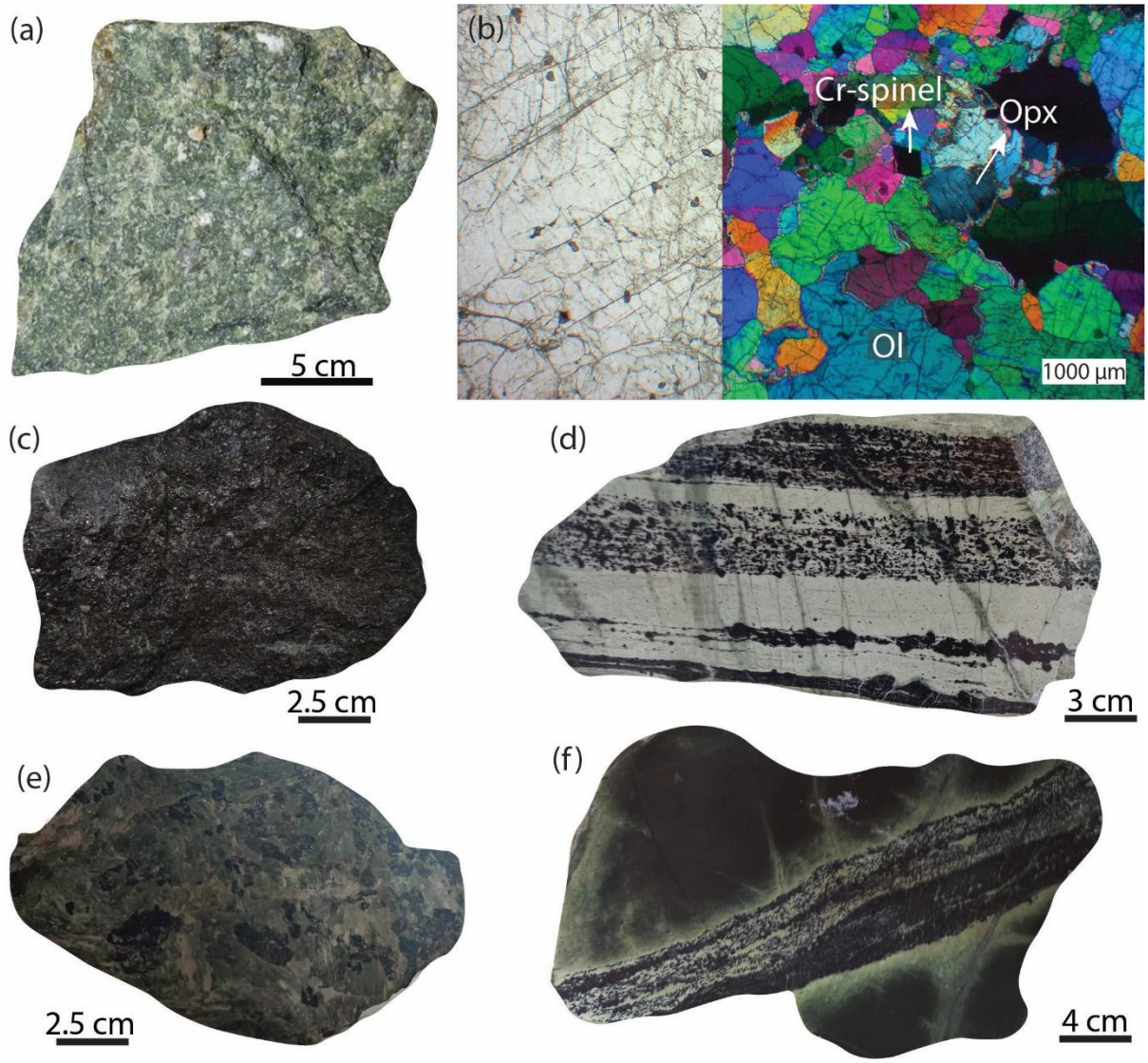

Figure 2. Harzburgite a) hand sample and b) thin section under parallel and cross-polarized light from the Me Maoya massif. b) Hand sample of chromitite collected from the Tiébaghi massif. Other textures observed in the old Tiébaghi chrome mine: c) small nodular chromitite interlayered with dunite crosscut by venules, d) pargasite-rich peridotite, f) Cr-rich rock crosscut by small chromitite nodules and hydrous silicates venules. Fig. 2e, f and g are photographs of the Museum collection at the Tiébaghi Village.

4. Methods

Both samples were sent for mineral separation at the Institute of Multipurpose Utilization of Mineral Resources (Chinese Academy of Geological Sciences in Zhengzhou). The ultraclean mineral separation workflow, which included gravimetric, magnetic, and

electrostatic separation, was designed to recover rare mineral occurrences found in ophiolites such as rutile and zircon (Appendix A). To prevent contamination, all equipment and worksites were thoroughly cleaned prior to processing. For further information on the mineral separation workflow refer to Appendix A.

4.1. Mineral characterization

Minerals of interest were picked and photographed with a Leica EZ4HD stereo microscope in a glass petri-dish.

4.1.1. Raman

Minerals were characterized using the Renishaw inVia confocal Raman microscope and spectrometer at The University of Queensland's Centre for Microscopy and Microanalysis. The system was calibrated with a silicon wafer (520.5 cm^{-1}) at the start and end of each session. Raman spectra were collected using a 514.5 nm laser and 50x objective, with a range of 100 to 2000 cm^{-1}, at room temperature (refer to Appendix A for Raman spectra).

4.1.2. Scanning Electron Microscopy (SEM) and energy dispersive X-ray (EDX) mineral analysis

Mineral grains were mounted in 2.54 cm epoxy resin discs and polished to reveal their crystal cores. Backscatter and CL SEM images and EDX data were obtained using a TESCAN Integrated mineral analysis (TIMA) Field Emission SEM at the Central Analytical Research Facility (Queensland University of Technology) or a Hitachi SU3500 at the Centre for Microscopy and Microanalysis (UQ). These data were used to examine mineral morphology, texture, fractures, and inclusions. CL images were obtained with a 10 Kv acceleration voltage and 12 nA beam current (Refer to Supplementary Material 1 for CL images). For identification of mineral phases on the TESCAN TIMA, the dot mapping approach was employed with 25 KV acceleration voltage, 1 μm/pixel spacing for backscatter imaging, 3 μm/pixel EDS dot spacing, and 1000 counts per spectrum per pixel analyzed. Mineral phases were identified based on EDX data using the TIMA software, and each assignment was verified to ensure correct overlap between the acquired data and the software database.

4.2. U-Pb age determination

U-Pb isotopes for zircon, rutile, and anatase grains were determined using the Thermo Fisher iCAP RQ quadrupole ICP-MS with an ASI RESOlution SE 193 nm laser (LA-ICP-MS) at the Centre for Geoanalytical Mass Spectrometry (CGMS) at the University of Queensland. U/Pb age analyses for zircons were conducted using 91500 zircon as the primary standard (Wiedenbeck et al., 1995) and Temora 2 grains (Black et al., 2003) as the secondary standard to monitor precision and accuracy, which was found to be better than 0.3% (Appendix A). Crystals were ablated using a 38 μm spot size beam in 22 cycles of 1s, with a repetition rate of 7Hz and fluence of 6J/cm^3. Only zircons with U/Pb ages with concordance between 90 – 110 % (^{206}Pb/^{238}U vs ^{207}Pb/^{235}U) were used for age calculations. Tera-Wassenburg and Kernel density diagrams were plotted with 2□ error using the Isoplot-R software (Vermeesch, 2018).

For U-Pb isotope measurements, rutiles and anatases were ablated using a 38 μm spot size beam in 22 cycles of 1s, a repetition rate of 8Hz and fluence of 3J/cm^3. The primary and monitoring standards were R632 (Axelsson et al., 2018) and DXK rutiles (Shi et al., 2012), respectively, and the precision and accuracy of these standards was less than 1% (Appendix A). Raw data were processed using Iolite software (Paton et al., 2011). Common Pb was corrected using the R632 standard and the "VizualAge UcomPbine" package (Chew et al., 2014) with the ^{208}Pb (no Th) correction. Out of the 230 grains analyzed, only 11 displayed Th values above 1 ppm, and most grains contained Th abundances below the detection limit. Consequently, the ^{208}Pb measured in these grains was assumed to be non-radiogenic (Zack et al., 2011).

Common Pb correction of unknown samples was achieved by grouping the samples based on their ^{206}Pb/^{238}U ages and plotting them in Tera-Wasserburg diagrams using ^{238}U/^{206}Pb and ^{207}Pb/^{206}Pb ratios (2σ propagated error) with Isoplot-R software (Vermeesch, 2018). Rutile ages presented in this study plots near the concordia line, indicating low levels of common lead in these grains. Concordia and lower intercept discordia ages exhibit a concordance rate of over 97%, facilitating age calculations. Final regression lines in the Tera-Wasserburg plots were unanchored for common Pb. To validate the common lead correction, three methods - nominal (0.9), Stacey-Kramer, and Isochron - were tested. Results showed that the isochron method was more consistent with low intercept ages calculated with unanchored common Pb. As a result, the isochron method was employed for age calculations and to plot data in kernel density plots.

4.3. Trace element abundance

Analyses of zircon trace element isotopes (^{91}Zr, ^{45}Sc, ^{49}Ti, ^{88}Sr, ^{89}Y, ^{93}Nb, ^{139}La, ^{140}Ce, ^{141}Pr, ^{146}Nd, ^{147}Sm, ^{153}Eu, ^{157}Gd, ^{163}Dy,^{172}Yb, ^{175}Lu, ^{178}Hf, ^{204}Pb, ^{206}Pb, ^{207}Pb, ^{208}Pb, ^{232}Th, ^{238}U) were performed within the same analytical session as those for U/Pb isotopes measurements. NIST612 glass standard was used as the primary standard, with NIST614 glass measured for quality control. Raw data were reduced using the Iolite software (Paton et al., 2011) with Zr as internal normalization standard.

Rutile and anatase were analysed for specific elemental abundances (**^{25}Mg, ^{27}Al, ^{45}Sc, ^{49}Ti, ^{51}V, ^{53}Cr, ^{55}Mn, ^{57}Fe, ^{59}Co, ^{60}Ni, ^{63}Cu, ^{88}Sr, ^{89}Y, ^{90}Zr, ^{93}Nb, ^{119}Sn, ^{121}Sb, ^{137}Ba, ^{139}La, ^{140}Ce, ^{141}Pr, ^{146}Nd, ^{147}Sm, ^{151}Eu, ^{157}Gd, ^{163}Dy, ^{172}Yb, ^{175}Lu, ^{178}Hf, ^{181}Ta, ^{182}W, ^{200}Hg, ^{206}Pb, ^{207}Pb, ^{208}Pb, ^{232}Th, ^{238}U) with the same Thermo Fisher iCAP RQ quadrupole ICP-MS with an ASI RESOlution SE 193 nm laser, but in a different analytical sessions as those for U/Pb isotope analyses. Trace element abundances of rutile and anatase grains were acquired using a 50 μm spot size beam that overlapped the U/Pb laser holes. Measurements were performed in 29 cycles of 1s at a frequency of 6 Hz and fluence of 3J/cm^3. NIST 612 and NIST 614 were used as primary and monitoring standards, respectively. Raw data were processed using the Iolite software (Paton et al., 2011) with Ti as the internal normalization standard. Trace elemental data of the primary standard (R632 rutile) display good agreement with the values obtained by Axelsson et al. (2018), indicating an accurate analytical session. For more information on analytical procedures, data acquisition, reduction, and validation, refer to Appendix A. Data are presented on a spreadsheet in Appendix B.

5. Results

Grains of zircon and the TiO_2 polymorphs rutile, and anatase were recovered from both the Me Maoya harzburgite and Tiébaghi chromitite (Fig. 3), each exhibiting unique characteristics depending on their host rock (Appendix A: A.Figs. 4-12; A.Table 1-2).

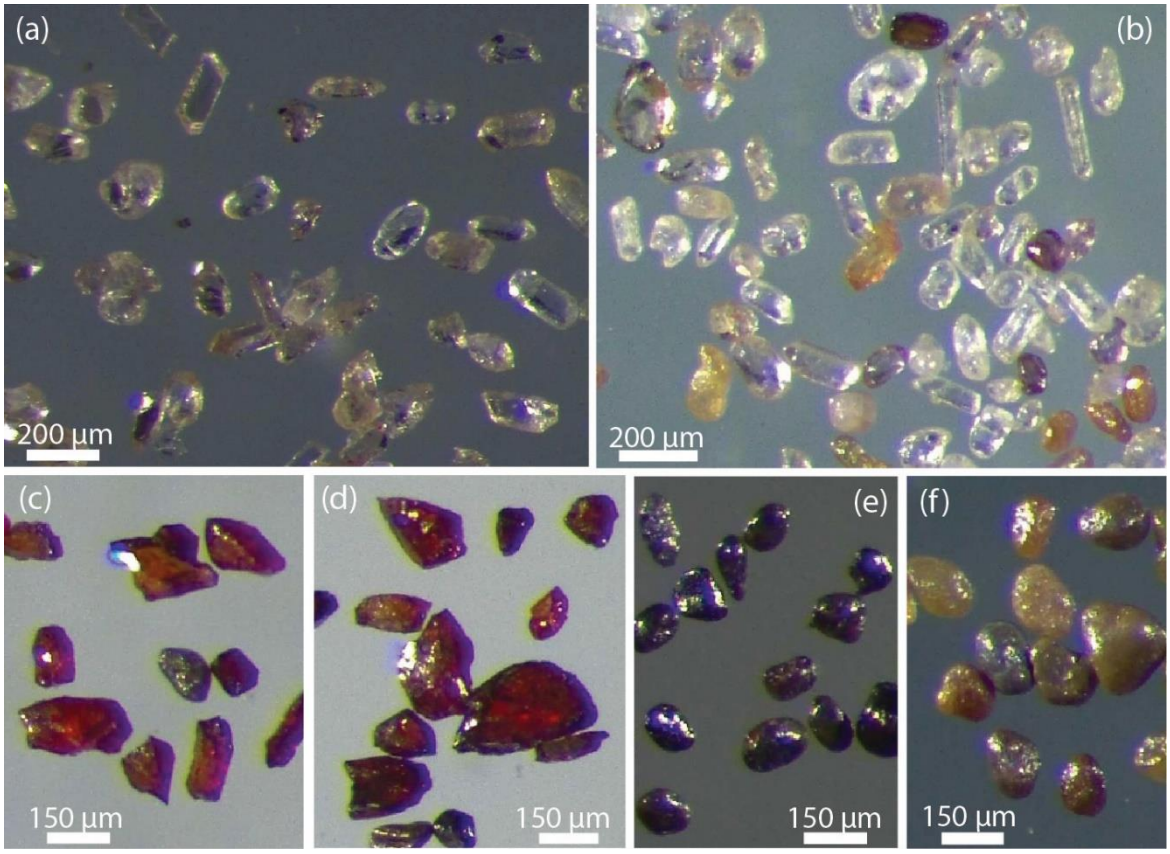

Figure 3. a) Homogenous zircon grains extracted from the Tiébaghi chromitite and b) heterogenous and rounded zircon grains from the Me Maoya harzburgite under binocular microscope. Red rutile grains extracted from c) Tiébaghi chromitite and d) Me Maoya harzburgite. e) rounded dark grey rutile and f) anatase grains recovered from the harzburgite.

5.1. Zircons

5.1.1. Morphology

Recovered zircons display a broad spectrum of colours and shapes, ranging from rounded to prismatic, with varying length:width aspect ratios (1-4) and CL properties. Grains extracted from the chromitite sample (approximately 60) are generally transparent and prismatic in shape, with low length-to-width ratios (2.5-1) and weak oscillatory or sector zoning CL. These zircons are commonly associated with serpentine, which occurs either filling cracks or surrounding the grains, as well as with Ca-Ti-bearing amphibolite (kaersutite), chromite, diopside, and enstatite (A.Fig. 11). In comparison, zircon grains from the harzburgite sample (approximately 280) are more diverse, showing varying colours (clear, yellow, red, dark red), shapes (rounded, subrounded, and prismatic double terminated) (Fig. 3), elongation (1-5), and CL (ranging from strong and fine oscillatory, weak to faint, and sector zoning). Additionally, the harzburgite zircon grains reveal mineral associations with

distinct crustal minerals, such as inclusions of quartz, rutile, diopside, and xenotime (A.Fig. 12).

Zircon grains can be grouped based on their U/Pb ages (A.Table 1). In general, those within the same age group exhibit similar features, such as Late Cretaceous zircons (90-120 Ma) that are characterized by subrounded morphology, low elongation, and prominent oscillatory zoning. While some grains display distinct characteristics within each different age group, the dominant features are presented in A.Table 1 for the purpose of characterization.

5.1.2. U-Pb ages

Amongst the 59 zircon grains from the Tiébaghi chromitite, 57 yielded concordant U/Pb ages ($^{206}Pb/^{238}U$ vs $^{207}Pb/^{235}U$; 90-110% concordance) spanning from 45 to 546 Ma (Fig. 4a). Most (n = 46) have an Eocene age (ca. 46.84 ± 0.22 Ma; MSWD = 0.92) and median Th/U ratio of 0.63. Other zircon grains yield the following ages: ~150 Ma (n = 6; Th/U^{avg} = 0.73), ~240 Ma (n = 2; Th/U = 0.38 and 0.49), ~405 Ma (n = 1; Th/U = 0.38), and ~560 Ma (n = 2; Th/U = 0.51 and 1.1).

Analyzed zircons grains from the Me Maoya harzburgite (n=276) yield 243 concordant U/Pb ages ($^{206}Pb/^{238}U$ vs $^{207}Pb/^{235}U$) ranging from 50 to 2764 Ma. U/Pb age populations can be visualized in kernel density plots (Fig. 4c, d). Phanerozoic ages predominate, with the most prominent age populations being Late Cretaceous (90-120 Ma; Th/U^{avg}=0.87), Early Jurassic to Cretaceous (125-170 Ma; Th/U^{avg} = 0.58), Late Permian to Early Triassic (225-260 Ma; Th/U^{avg} = 0.61), and Late Ordovician to Early Devonian (405-465 Ma; Th/U^{avg} = 0.38). Some rare zircons have ages dating from the Neo-, Meso-, and Paleoproterozoic eras, and one Archean zircon is noted. The largest Proterozoic age cluster lies within the Stenian-Tonian periods (ca. 945 Ma). A single zircon from the harzburgite yielded an Eocene age (49.9 ± 1.4 Ma; Th/U = 0.7), which is similar to the young age cluster observed in zircons from the chromitite.

5.1.3. Trace element abundances

Individual age populations have distinct chemical signatures. Eocene zircons are characterized by lower Ti (13 ppm), Nb (1.1 ppm), U (182 ppm) and higher Sc (94 ppm), Y (4105 ppm), Gd (55 ppm), Dy (295 ppm), Yb (1683 ppm), and Lu (1683 ppm) median values. In contrast, other Phanerozoic populations display median trace elemental values in the range of (in ppm): Ti 16-58, Nb 2.5-5, U 404-720, Sc 59-70, Y 1500-2000, Gd 27-37, Dy

135-163, Yb 500-685, and Lu 82-130. Phanerozoic zircons are comparable to those from continental arc or mid-ocean ridge settings (Grimes et al., 2015; Figs. 5a, b). In contrast, the Eocene population plots outside the mantle zircon array and differs from zircons analyzed from other tectonic setting fields (Fig. 5). This younger population is characterized by significant depletion in Nb and anomalously high Yb values, leading to low U/Yb, Gd/Yb, Sc/Yb, and Nb/Yb ratios. This distinction is also evident in the trace and rare-earth element chondrite-normalized plots (Fig. 5c, d) on which Eocene zircons exhibit marked depletion in U, Pb, Nb, La, and enrichment in middle to heavy rare-earth elements (Eu, Gd, Dy, Y, Yb, Lu) and Sr as compared to other zircon age groups.

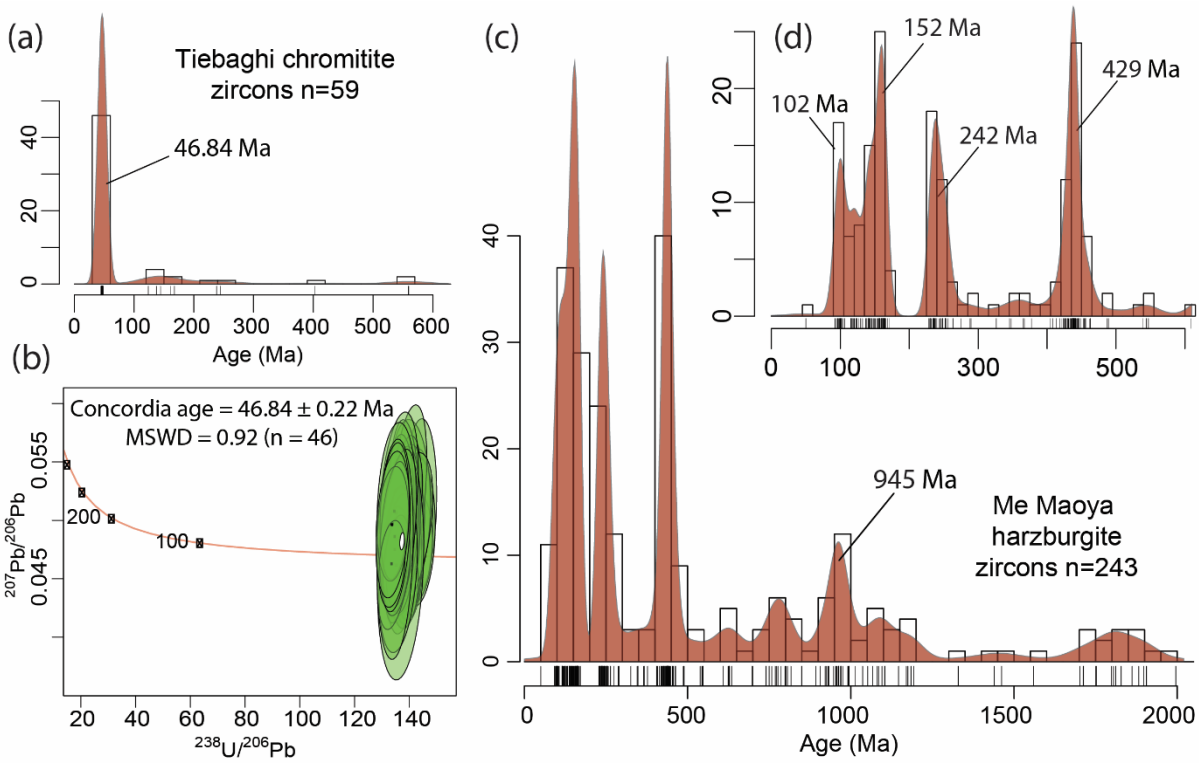

Figure 4. Zircon U-Pb age determinations. a) Kernel density plot exhibiting distribution of U238/Pb206 zircon ages and b) Tera-Wasserburg plot showing youngest zircon population from the Tiébaghi chromitite sample. c) Kernel density plot showing distribution of U238/Pb206 zircon ages from Me Maoya harzburgite and inset d) zircon showing populations <600 Ma. Diagrams were plotted using IsotplotR (Vermeesch, 2018) and the ages of the peaks were calculated using the software Density plotter (Vermeesch, 2012)

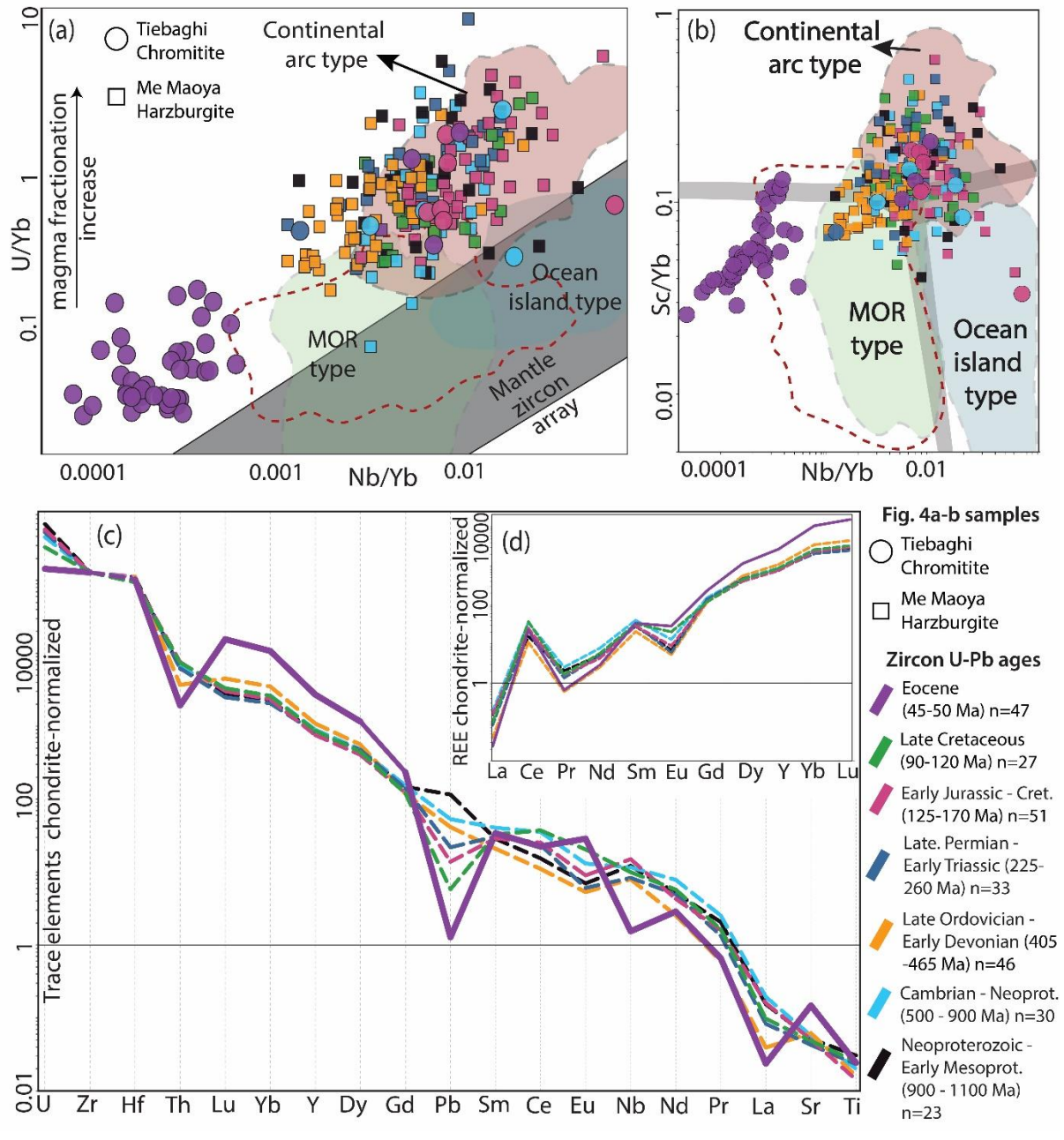

Figure 5. Plots of trace element abundances in zircons differentiating potential tectono-magmatic sources and settings. a) U/Yb vs Nb/Yb diagram and b) Sc-Nb/Yb plot (diagrams and fields are after Grimes et al., 2015 and references therein). Trace element (c) and REE chondrite-normalized (d) diagrams (chondrite values are after Sun and McDonough, 1989) for zircons. Lines display the median values of each zircon population grouped according to their ages.

5.2. *TiO_2 polymorphs*

5.2.1. *Morphology*

Red rutile grains from both samples are relatively uniform under both reflective light and backscatter imaging (Appendix A). They exhibit length (c-axis) of 50 to 250 μm and

prismatic to rounded morphology. These rutile grains generally show homogenous zoning and massive textures, but partial to pervasive dissolution features are also present. Those extracted from the chromitite exhibit common mineral association with serpentine, which appears encompassing (A.Fig. 11) or filling fractures. Other associations include biotite and garnet at the rim and micro- to nanometer-sized ilmenite exsolutions. In contrast, red rutile grains recovered from the harzburgite exhibit less common associations with serpentine but exhibit a diverse range of inclusions and mineral associations, such as titanite, albite, ilmenite, amphibole, corundum, plagioclase, diopside, and quartz (A.Fig. 12).

Dark grey rutile grains occur in the Me Maoya samples and have lengths of 75 to 220 μm and subrounded to rounded morphology. They variably display homogenous to poikilitic textures, with the most common mineral associations being zircon and quartz (A.Fig. 12).

Anatase grains occur in the Me Maoya samples and are 75 to 210 μm in length and have subrounded to rounded morphology (A.Fig. 10). They exhibit massive to poikilitic textures and mineral associations with zircon, quartz, muscovite, and titanite (A.Fig. 12). The characteristics of the Ti-oxide phases are summarized in the Appendix A (A.Table 2).

5.2.2. U-Pb ages

Ages of red prismatic rutiles from both chromitite and harzburgite samples have been reliably determined and range from Devonian to Eocene. U-Pb age determinations for red rutile grains (n = 82) from the chromitite sample exhibit well-defined populations, including an Eocene cluster at ~47 Ma (as determined by the lower intercept age; Fig. 6a, c), Late-Triassic to Early-Jurassic grains peak around 200 Ma, and an older Early-Devonian population occurs at approximately 400 Ma. Similar age clusters are also observed amongst the analyses of red rutile grains (n = 150) from the harzburgite, without any Eocene ages. A more refined age distribution near 200 Ma is seen in rutile grains from the harzburgite (Figure 6b), however, this may be an artifact of data clustering. Therefore, the cluster at 205 Ma, is considered to overlap with rutile U/Pb ages from the Tiebaghi chromitite, providing a more consistent and reliable age for geological interpretations.

In contrast, anatase and dark grey rutile grains exhibit higher Th and common Pb concentrations, making data reduction and age estimation more challenging. Despite these difficulties, a lower intercept discordia age of approximately 230 Ma can be estimated for the dark-grey rutiles and although it should be interpreted with caution it may have geological significance (Appendix A - A.Fig 15). In contrast, U-Pb data obtained from anatase grains did not yield any reliable ages due to the high and non-linear concentration of common Pb.

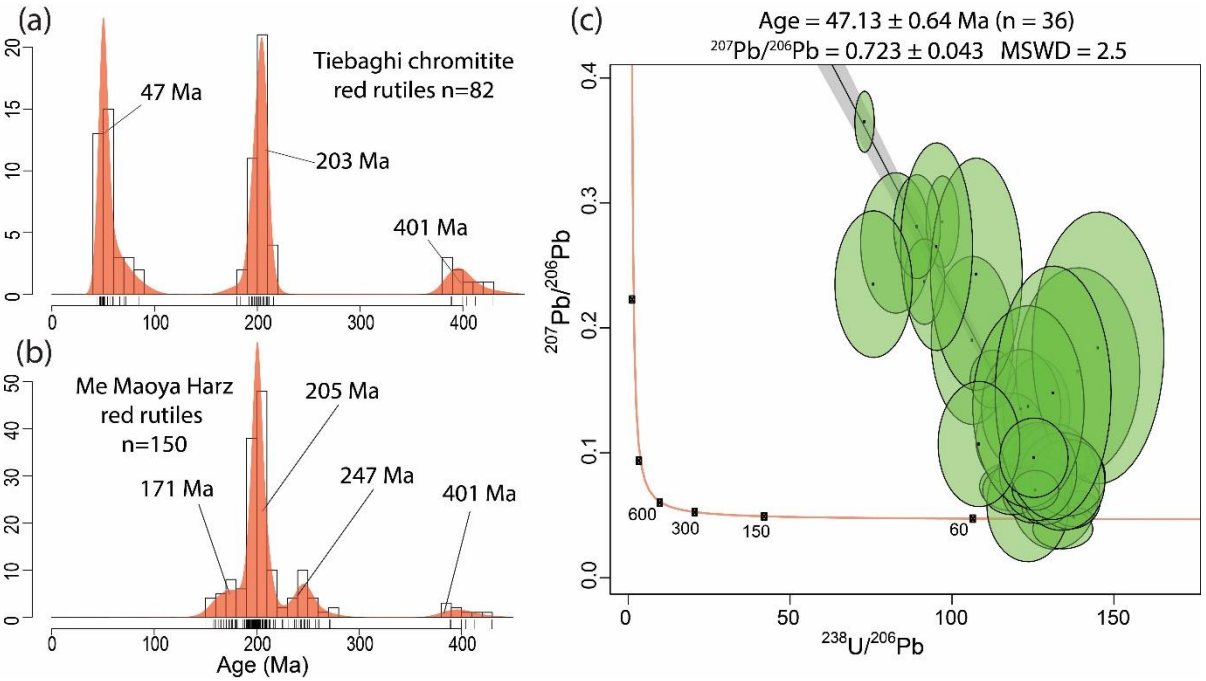

Figure 6. U-Pb age determinations for red rutiles calculated using $^{238}U/^{206}Pb$ vs $^{207}Pb/^{206}Pb$ ratios. Ages are corrected for common Pb using the Isochron method. Kernel density plots exhibiting U-Pb rutile ages from a) chromitite and b) harzburgite. c) Tera-Wasserburg plot showing the youngest rutile population (only observed in the chromitite sample). Diagrams were plotted using IsotplotR (Vermeesch, 2018) and the ages of peaks were calculated using the software Density plotter (Vermeesch, 2012).

5.2.3. Trace element abundances

Red rutile populations can be further differentiated according to their trace element abundances (Fig. 7, 8). Eocene grains exhibit a distinct chemical composition, characterized by higher Sc (3 ppm), Cr (4000 ppm), Zr (1200 ppm), and Hf (55 ppm), and lower V (1480 ppm), Al (131 ppm), and Fe (590 ppm) values compared to other age groups. Red rutile clusters ca. 205 and 400 Ma ages have mean elemental contents ranging from Sc 0.4 - 0.9 ppm, Cr 265 - 2293 ppm, Zr 272 - 380 ppm, Hf 12 - 17 ppm, V 2300 - 3700 ppm, Al 180 - 370 ppm, and Fe 1500 - 3500 ppm. In contrast, dark grey rutile and anatase grains reveal significantly higher abundances of Ta, Nb, and REEs in comparison to all red rutile grains.

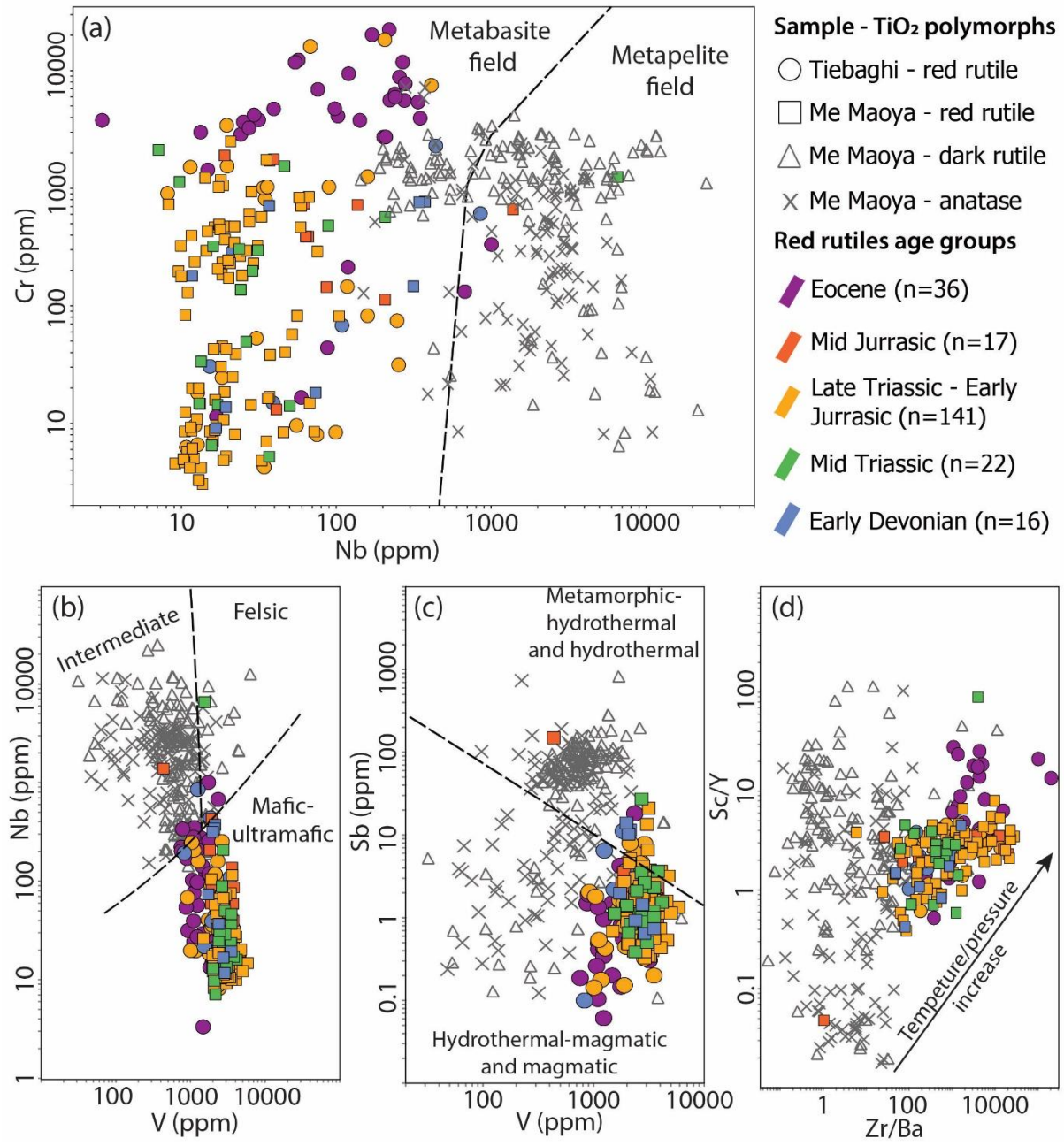

Figure 7. Trace element plots for rutile and anatase. a) Cr vs Nb (ppm) diagram (Triebold et al., 2012) exhibiting concentration of red rutile in the metabasite field, while anatase and dark rutile plot within the metapelite field. b) Nb vs V (ppm) plot showing likely source rock types for distinct rutile and anatase grains. c) Sb vs V (ppm) plot showing most red rutiles plotting within the hydrothermal-magmatic/magmatic field, whereas anatase and dark grey rutile concentrate mostly in the metamorphic/hydrothermal field. d) Sc/Y vs Zr/Ba diagram exhibiting the tendency of red prismatic rutile to be associated with higher temperature/pressure conditions than anatase and dark grey rutile. Fields and trend arrows for diagrams b, c and d are after Sciuba and Beaudoin (2021).

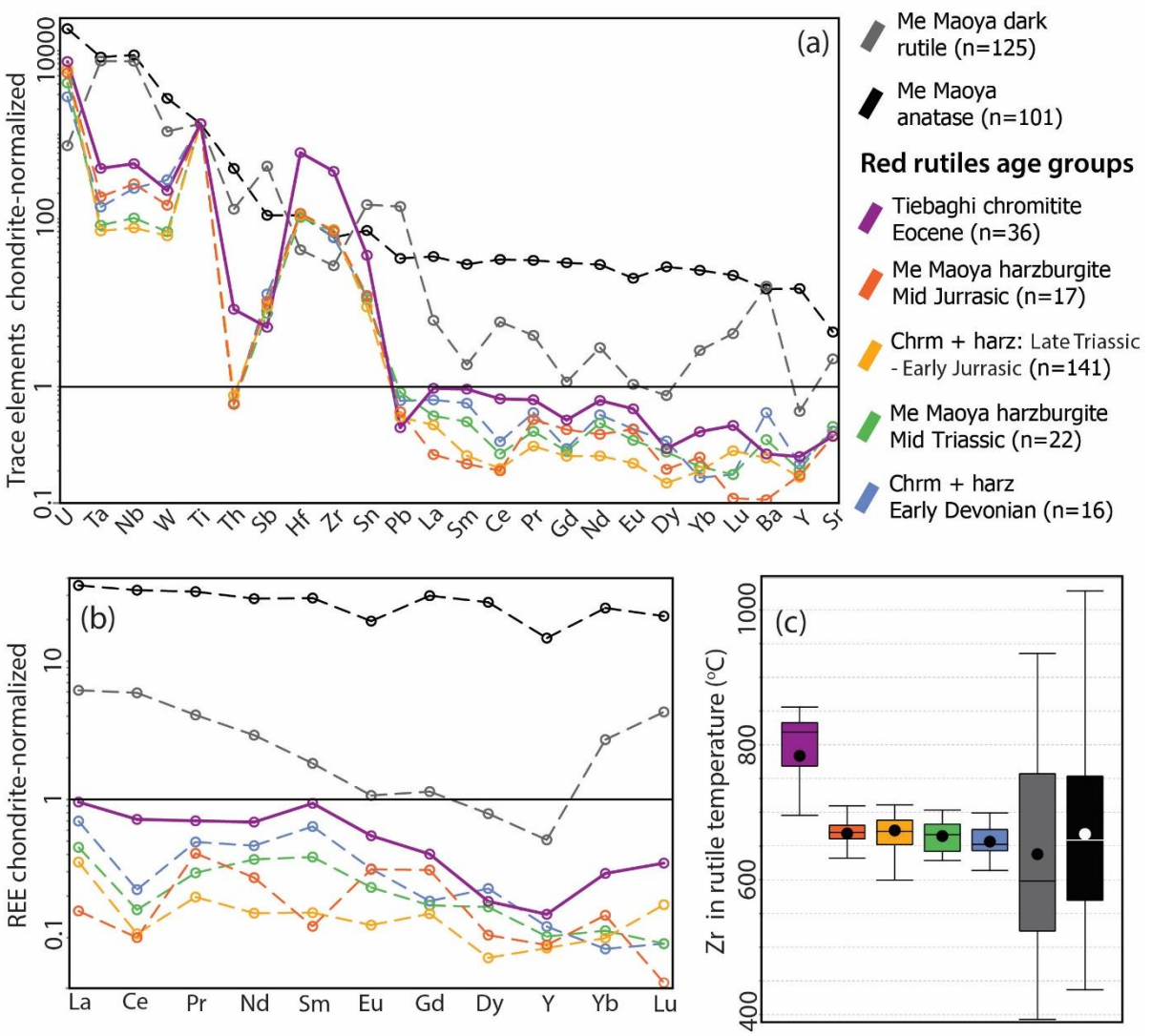

Figure 8. Chondrite-normalised trace element (a) and REE (b) median values (chondrite values are from Sun and McDonough, 1989). c) Crystallization temperatures of rutile and anatase grains calculated according to the Zr in rutile thermochronometer (Tomkins et al., 2007) (bottom and top of the box = Q3 and Q1, respectively; black dot – mean; line – median).

6. Discussion

6.1. Origin of zircons

6.1.1. U-Pb age constraints

The largest (80% of concordant analyses) and youngest population of zircons comes from the Tiébaghi chromitite sample and yields an Eocene age (ca. 46.84 ± 0.22 Ma; MSWD = 0.92) with 2□ error of the 48 Ma age reported for zircons from the same sample that were analysed by SHRIMP at Australian National University (Aitchison et al., 2022). A solitary zircon grain from the Me Maoya harzburgite also yielded an Eocene age (49.9 ± 1.4 Ma) that

454 is again within 2□ error of the 48 Ma age reported from Tiébaghi chromitite by Aitchison et
455 al. (2022). These younger ages are interpreted as approximating the last magmatic event
456 during which the collected samples were exposed.
457 Accordingly, zircons older than the Eocene population recovered from both the
458 chromitite and harzburgite samples are interpreted as xenocrysts. These inherited grains are
459 relatively rare in the chromitite sample (n = 10), but they are more abundant in the
460 harzburgite (n = 246). Their ages tend to cluster within discrete populations in the
461 Phanerozoic and are more dispersed in the Precambrian. Late-Cretaceous grains (120-90 Ma)
462 are generally rounded, have low elongation, and fine oscillatory zoning, suggesting a likely
463 derivation from terrigenous sediments. Their ages are similar to zircons from the Formation à
464 charbon (Aitchison et al., 1998; Adams et al., 2008; Cluzel et al., 2011), and partially
465 overlaps with those of from the Kone Facies within the Poya terrane (Cluzel et al., 2018) and
466 Boghen terrane (Adams et al., 2009) in New Caledonia (Fig. 9).
467 Other zircons with older Mesozoic ages (Early Jurassic to Cretaceous; 170-125 Ma)
468 exhibit similarities within the age range of the population known from the Boghen terrane
469 (Cluzel and Meffre, 2002; Adams et al., 2009). Late Permian-Early Triassic (260-225 Ma)
470 zircon ages overlap most closely with those of detrital zircons from volcaniclastic sediments
471 of the Téremba and Koh-Central terranes (Adams et al., 2008; Campbell et al., 2018; Fig 9).
472 However, some of these and older zircon xenocryst populations appear to slightly deviate
473 from the depositional or magmatic ages observed in the basement terranes of New Caledonia
474 (Fig. 9). For example, zircons of Late Ordovician to Early Devonian age predate the oldest
475 rocks in New Caledonia. Potentially, however, these grains represent inherited components of
476 the detrital zircon populations within clastic units amongst these younger terranes. Indeed,
477 similar ages have been reported from Koh-Central and Téremba terranes (Aitchison et al.,
478 1998; Adams et al., 2008; Campbell et al., 2018).
479 To gain a comprehensive understanding of detrital inheritance, it is essential to
480 examine New Caledonia within the paleogeographic context of the eastern Gondwana
481 (Australian) margin before the Zealandia rifting and the opening of the Tasman and Coral
482 seas. Previous studies have established correlations between Permian to Mesozoic rocks in
483 the New Caledonian basement and those along the Eastern Gondwana margin (Aitchison et
484 al., 1998; Cluzel et al., 2012b; Campbell et al., 2018). Zircon detrital studies conducted on
485 Late Permian to Early Triassic units of the Murihiku, Caples (New Zealand) and Gympie
486 terranes (Eastern Australia) reveal closer similarities with the corresponding zircon xenocryts
487 found within the New Caledonia ophiolite. Additionally, presence of Late Permian-Early

Triassic zircon xenocrysts, falling within the Devonian to Triassic age range of widespread felsic magmatic rocks along the New England Orogen in eastern Australia (Murray et al., 1987; Glen, 2005; Rosenbaum et al., 2020), suggest this possible correlation with eastern Australian Gondwana margin. This correlation is further supported by matching ages of Late Ordovician-Early Devonian (465-405 Ma) zircon xenocryst ages and the occurrence of extensive S- and I-type granite intrusions in the Lachlan Fold Belt of NSW (Kemp et al., 2009). Thus, input of sediments into the basins that developed on the Zealandia continent prior to its separation from eastern Australia, supported by extensive zircon U-Pb detrital studies in New Caledonia and New Zealand (Aitchison et al., 1998; Adams et al., 2008, 2022; Cluzel et al., 2011; Campbell et al., 2018), may contribute as sources of these xenocryst. Moreover, these findings highlight the capability of such xenocrysts to elucidate paleogeographic constraints associated with the development of the ophiolite.

6.1.2. Trace element geochemistry constraints

Zircon geochemical analyses offer a promising approach for identifying the sources of xenocrysts together with their U-Pb ages. Examination of zircon trace elements reveals that the majority of xenocrysts originate from crustal sources. Notably, the trace element signatures of Late Permian-Early Triassic zircon xenocrysts exhibit similarities to those observed in rocks derived from continental arcs. This resemblance aligns with the volcanoclastic rocks discovered in the Téremba terrane, which are interpreted as sediments resulting from the deposition in a continental margin forearc basin associated with arc magmatism (Aitchison et al., 1998; Adams et al., 2009b), or zircon trace elemental data from rocks of the Murihiku terrane in New Zealand (Campbell et al., 2020b) thus providing support for these rocks being plausible xenocryst sources. Moreover, trace element analysis of zircon xenocrysts from the Early Paleozoic, which display similarities to continental rocks, coupled with their positive $\delta^{18}O$ values and negative $\varepsilon Hf_{(t)}$ values, are consistent with zircons found in S-type granites of similar ages documented in the Lachlan orogen (Kemp et al., 2009).

Furthermore, comparing the geochemical characteristics of Eocene zircons from the chromitite with xenocryst populations and zircons formed in different tectonic settings (Fig. 5) highlights distinct processes responsible for the formation of the younger zircon population. These mechanisms likely entail intricate interactions between the depleted host rock and new melt injections. Throughout this process, specific elements may have been selectively distributed among other coeval phases, leading to the atypical geochemical

attributes observed in these Eocene zircons (e.g., Nb depletion attributed to higher partitioning into contemporaneous rutile phases).

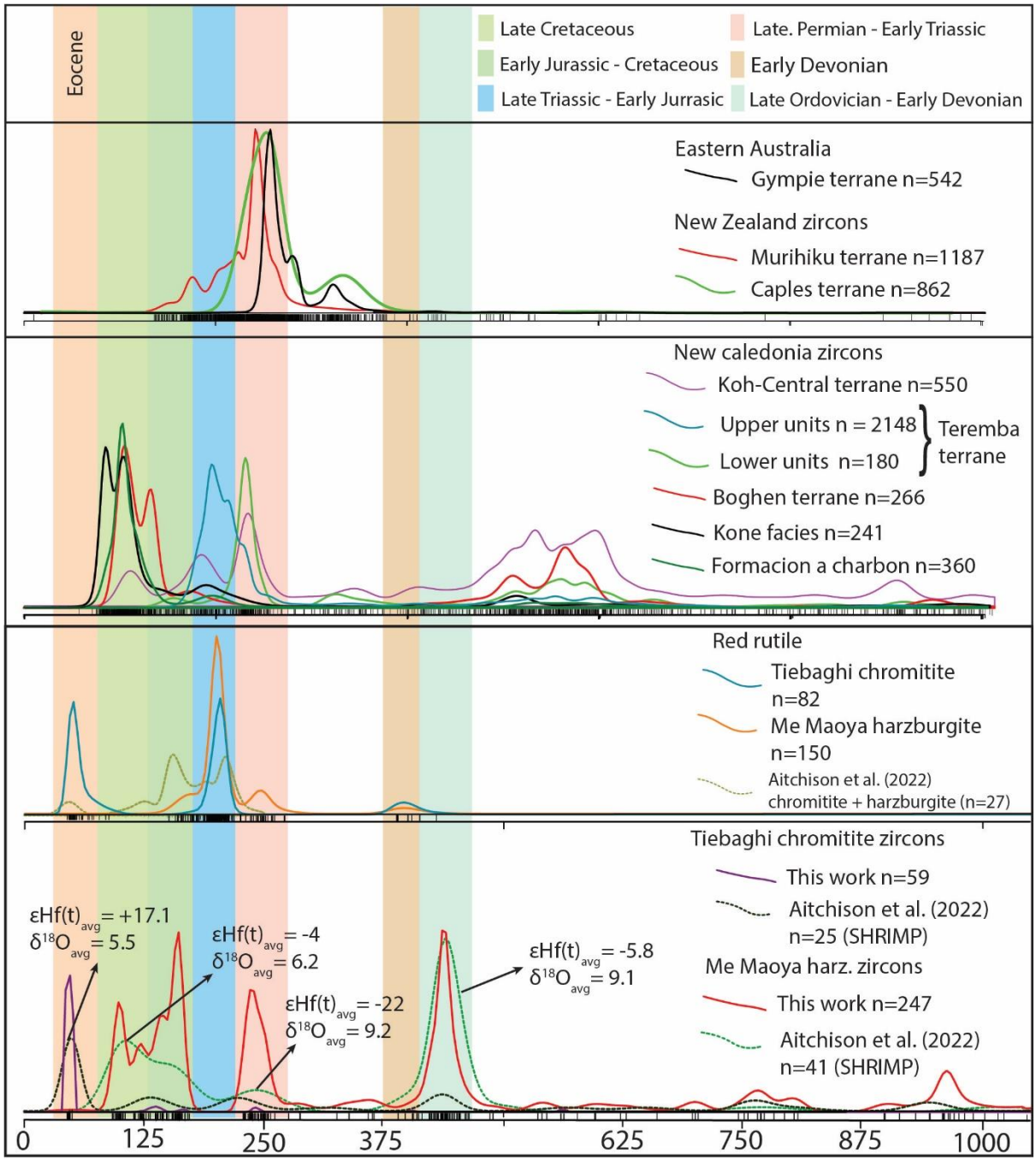

Figure 9. Kernel density plot of age distributions for zircon and rutile recovered from harzburgite and chromitite samples compared to possible sources in New Caledonia and Eastern Australia. Peritotite Nappe zircon (U-Pb, εHf and $\delta^{18}O$) and U-Pb rutile ages after Aitchison et al. (2022); Detrital zircon compilation: Boghen terrane (Adams et al., 2009); Kone Facies (Cluzel et al., 2018); Formation à charbon (Adams et al., 2008; Cluzel et al., 2011); Koh-Central terrane (Adams et al., 2008; Campbell et al., 2018); Teremba terrane (Adams et al., 2009b; Campbell et al., 2018); Gympie terrane (Rosenbaum et al., 2020); Muhiriku terrane (Adams et al., 2007; Campbell et al., 2020a); Caples terrane (Adams et al., 2009a).

6.2. Origin of TiO_2 polymorphs

Red rutiles recovered from both harzburgite and chromitite yield U-Pb ages that cluster in the Eocene (ca. 47 Ma) and Late Triassic-Early Jurassic (ca. 205 Ma), with less prominent peaks at 171, 247 and 401 Ma. Red rutile xenocrysts (> 53 Ma) exhibit geochemical signatures similar to those of mafic-ultramafic rocks and were likely originated through magmatic processes. These findings indicate these xenocrysts were likely recycled from mafic units within the subducting slab. In contrast, anatase and dark grey rutiles are similar to those of metapelitic rocks of intermediate composition that crystallized in metamorphic/hydrothermal conditions (Fig. 7). Furthermore, their anomalous REE abundances provide additional evidence for distinct sources or crystallization processes compared to the red rutile samples. Although reliable U-Pb ages could not be obtained for dark rutile and anatase grains, their geochemical signatures suggest the involvement of sedimentary rocks in the forearc mantle wedge.

Determination of the sources of TiO_2 xenocrysts remains challenging given the limited dataset for rutile U-Pb ages amongst potential source rocks in New Caledonia or other units along the Eastern Gondwana margin. These xenocrysts could have originated from the extensive mafic and intermediate rocks present in New Caledonia (Maurizot et al., 2020b) or other unidentified metasedimentary rocks. Their ages correlate with known metamorphic episodes affecting New Caledonian basement terranes (Aitchison et al., 2022) and New Zealand (Adams, 2003).

Additionally, these grains also display distinctions related to their crystallization temperature (Sc/Y vs Zr/Ba diagram – Fig. 7d), with higher temperatures indicated for red rutiles in comparison to anatases and dark rutiles. This is further supported by estimations of the crystallization temperature using the Zr-in-rutile thermometer (pressure = 15 Kbar and β-quartz field), with the Eocene cluster showing a pronounced mean crystallization temperature of 818 °C, compared to other minerals and age populations (Fig. 8c).

It is worth noting that Eocene red rutile grains (ca. 47 Ma) exhibit distinctive geochemical signatures. These rutiles display notable concentrations of high field strength elements (HFSEs), specifically Ta, Nb, Hf, and Zr (Fig. 8a), as well as higher abundances of rare earth elements (REEs) compared to the older red rutile clusters (Fig. 8b). These unique geochemical characteristics, combined with elevated Cr contents (4000 ppm), suggest that these grains likely formed within their chromitite host rock through percolation of late and geochemically enriched melts or fluids. Chromitite from the Tiebaghi massif, which displays

567 abundant evidence for fluid percolation in its petrography (Fig. 2), provides further support
568 for this interpretation.
569
570 **7. Conclusions**
571 Zircon and the TiO_2 polymorphs, rutile and anatase, occurring within the ultramafic
572 rocks of the Peridotite Nappe ophiolite exhibit unique textural, chemical, and isotopic
573 features. These mineral phases serve as valuable indicators for exploring the evolution of the
574 forearc mantle-wedge and associated geodynamic processes, including:
575 • Eocene zircon and rutile grains recovered from the Tiébaghi chromitite are both likely to
576 be of magmatic origin and associated with a late stage of melt or fluid percolation, as
577 evidenced by their association with alkali-hydrous silicate phases. Overlap between
578 Eocene U-Pb zircon and rutile ages, and Ar/Ar ages reported from pargasite (Cluzel et
579 al., 2022) indicates that the Tiébaghi chromitite had already cooled considerably by ca.
580 47-46 Ma, providing important constraints on the cooling period of ultramafic rocks
581 from the northern section of the Peridotite Nappe.
582 • Zircon grains older than the ophiolite crystallization age are interpreted as xenocrysts and
583 those as old as Permian exhibit similarities with units amongst the New Caledonian
584 basement terranes. Other older zircon populations are consistent with multi-cycle
585 derivation from the eastern Australian and New Zealand margin against which New
586 Caledonia was juxtaposed prior to Zealandia dispersal.
587 • The sources of rutile xenocrysts, which have U-Pb ages clustered in the Late Triassic-
588 Early Jurassic cannot be directly confirmed and likely fingerprint metamorphic event
589 within the regional geology evolution.
590 • The occurrence of zircon and rutile xenocrysts with pristine isotopic systems in mantle
591 rocks supports a hypothesis invoking recycling from the subducting lithospheric slab into
592 the mantle wedge occurring at shallow levels. To avoid thermal resetting of the U-Pb
593 radiometric clock, rutile xenocrysts must have been transferred at depths above 60-80 km
594 (Fig. 10). This likely occurred in combination with the dewatering of the subducting slab
595 and the release of fluids that hydrate the mantle wedge and trigger recycling processes.
596 • Mantle recycling process involving xenocrysts originating from the subducting slab are
597 considered to have occurred shortly during the initial stages of the ophiolite exhumation.
598 Xenocrysts were likely incorporated into the over-riding mantle wedge by fluid
599 percolation in between rock and mineral fractures.

The findings of this study have implications on the understanding of mantle recycling processes. Furthermore, they indicate the potential for detailed characterization of the wide variety of minerals that are present in ultramafic rocks rather than just zircon alone to investigate the evolution of forearc mantle wedge systems.

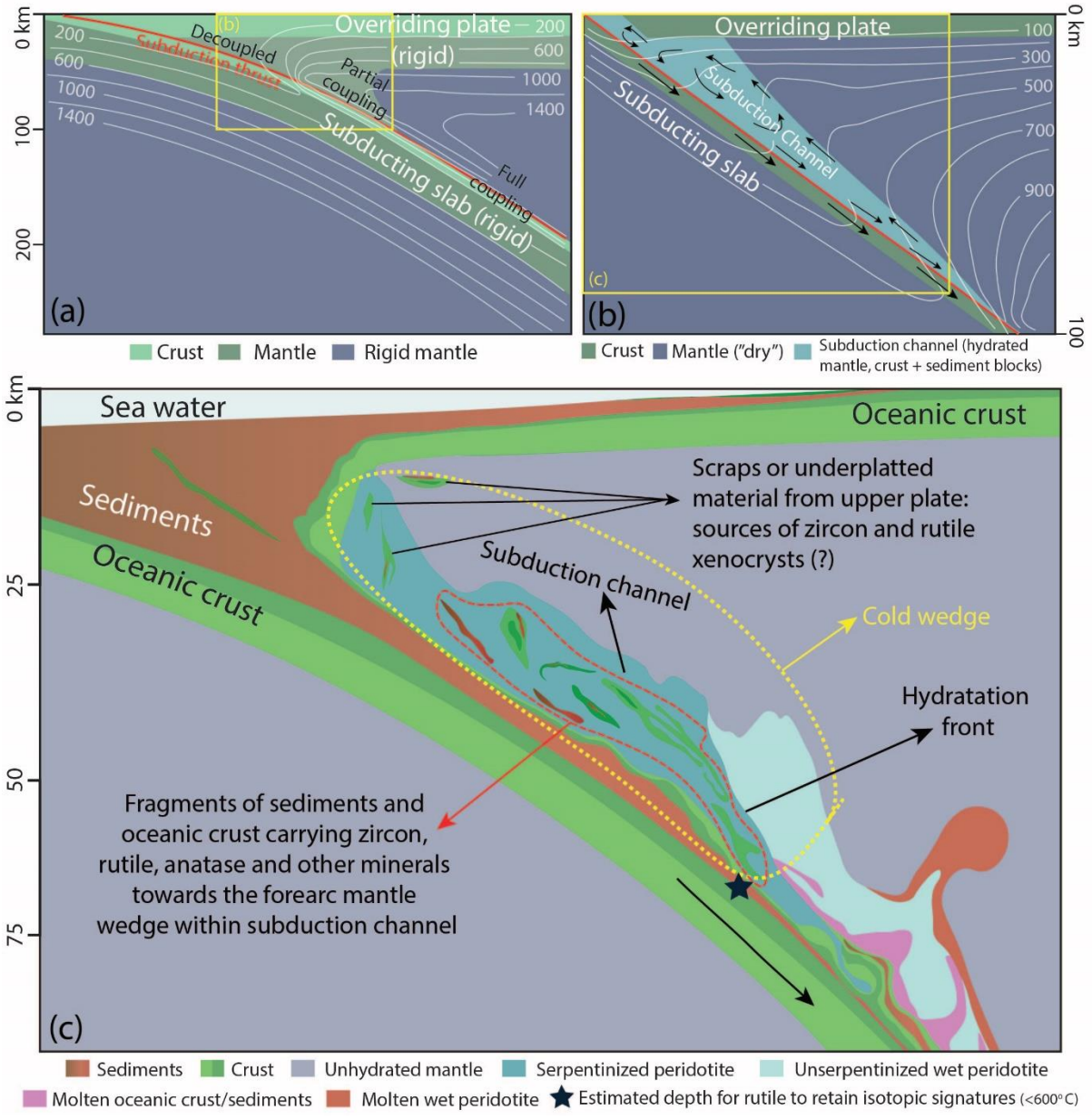

Figure 10. a) Geotherms of an intra-oceanic subduction system (adapted after Syracuse et al., 2010) b) Intra-oceanic model exhibiting the location and dynamics of a subduction channel (adapted after Gerya et al., 2002) c) Detailed model showing interpretation of how zircon, rutile and other materials are transferred and recycled into a forearc mantle-wedge; corrugations between the subducting material and the hydration front depict slab dehydration associated to metamorphic reactions (adapted after Gerya, 2011).

Acknowledgements

The authors acknowledge funding support from the Australian Research Council (ARC DP190100814 Diamonds in ophiolites: Recycling deep mantle into supra-subduction zones). D.C. and J.C.A. thank M. Henri Reuillard, M. Marc Akaro and the Tiébaghi Historical Society for arranging access to the mine wash plant and to Aileen and Elisabeth for help in sample collection.

618 **References**

619

620 Adams, C.J., 2003. K-Ar geochronology of Torlesse supergroup metasedimentary rocks in
621 Canterbury, New Zealand. Journal of the Royal Society of New Zealand 33, 165–187.
622 https://doi.org/10.1080/03014223.2003.9517726
623 Adams, C.J., Cambell, H.J., Griffin, W.L., 2007. Provenance comparisons of Permian to
624 Jurassic tectonostratigraphic terranes in New Zealand: Perspectives from detrital zircon
625 age patterns. Geological Magazine 144, 701–729.
626 https://doi.org/10.1017/S0016756807003469
627 Adams, C.J., Campbell, H.J., Griffin, W.J., 2008. Age and provenance of basement rocks of
628 the Chatham islands: An outpost of Zealandia. New Zealand Journal of Geology and
629 Geophysics 51, 245–259. https://doi.org/10.1080/00288300809509863
630 Adams, C.J., Campbell, H.J., Griffin, W.L., 2009a. Tracing the Caples terrane through New
631 Zealand using detrital zircon age patterns and radiogenic isotope signatures. New
632 Zealand Journal of Geology and Geophysics 52, 223–245.
633 https://doi.org/10.1080/00288300909509888
634 Adams, C.J., Cluzel, D., Griffin, W.L., 2009b. Detrital-zircon ages and geochemistry of
635 sedimentary rocks in basement Mesozoic terranes and their cover rocks in New
636 Caledonia, and provenances at the eastern Gondwanaland margin. Australian Journal of
637 Earth Sciences 56, 1023–1047. https://doi.org/10.1080/08120090903246162
638 Adams, C.J., Mortimer, N., Campbell, H.J., Griffin, W.L., 2022. Detrital zircon provenance of
639 Permian to Triassic Gondwana sequences, Zealandia and eastern Australia. New Zealand
640 Journal of Geology and Geophysics 65, 457–469.
641 https://doi.org/10.1080/00288306.2021.1954957
642 Agard, P., Prigent, C., Soret, M., Dubacq, B., Guillot, S., Deldicque, D., 2020. Slabitization:
643 Mechanisms controlling subduction development and viscous coupling. Earth-Science
644 Reviews 208, 103259. https://doi.org/10.1016/j.earscirev.2020.103259
645 Aitchison, J.C., Clarke, G.L., Meffre, S., Cluzel, D., 1995. Eocene arc-continent collision in
646 New Caledonia and implications for regional southwest Pacific tectonic evolution.
647 Geology 23, 161–164. https://doi.org/10.1130/0091-
648 7613(1995)023<0161:EACCIN>2.3.CO;2
649 Aitchison, J.C., Cluzel, D., Ireland, T.R., Zhou, R., Lian, D., Patias, D., Yan, Z., Yang, J.,
650 2022. Solid-phase transfer into the forearc mantle wedge : Rutile and zircon xenocrysts
651 fingerprint subducting sources. Earth and Planetary Science Letters 577, 117251.

652 https://doi.org/10.1016/j.epsl.2021.117251
653 Aitchison, J.C., Ireland, T.R., Clarke, G.L., Cluzel, D., Davis, A.M., Meffre, S., 1998.
654 Regional implications of U/Pb SHRIMP age constraints on the tectonic evolution of
655 New Caledonia. Tectonophysics 299, 333–343. https://doi.org/10.1016/S0040-
656 1951(98)00211-X
657 Avias, J., 1967. Overthrust structure of the main ultrabasic new caledonian massives.
658 Tectonophysics 4, 531–541. https://doi.org/10.1016/0040-1951(67)90017-0
659 Axelsson, E., Pape, J., Berndt, J., Corfu, F., Mezger, K., Raith, M.M., 2018. Rutile R632 – A
660 new natural reference material for U-Pb and Zr determination. Geostandards and
661 Geoanalytical Research 42, 319–338. https://doi.org/10.1111/ggr.12213
662 Baldwin, S.L., Rawling, T.J., Fitzgerald, P.G., 1999. Thermochronology of the northern high
663 P/T terrane of New Caledonia: implications for mid-Tertiary plate boundary process in
664 the SW Pacific. Penrose Conference. 13–14.
665 Black, L.P., Kamo, S.L., Allen, C.M., Aleinikoff, J.N., Davis, D.W., Korsch, R.J., Foudoulis,
666 C., 2003. TEMORA 1: A new zircon standard for Phanerozoic U-Pb geochronology.
667 Chemical Geology 200, 155–170. https://doi.org/10.1016/S0009-2541(03)00165-7
668 Campbell, M.J., Rosenbaum, G., Allen, C.M., Mortimer, N., Shaanan, U., 2020a. Episodic
669 behavior of the eastern Gondwanan margin: Insights from detrital zircon
670 petrochronology from the Murihiku Terrane, New Zealand. Lithos 356–357, 105367.
671 https://doi.org/10.1016/j.lithos.2020.105367
672 Campbell, M.J., Rosenbaum, G., Allen, C.M., Spandler, C., 2020b. Continental crustal
673 growth processes revealed by detrital zircon petrochronology: Insights from Zealandia.
674 Journal of Geophysical Research: Solid Earth 125, 1–23.
675 https://doi.org/10.1029/2019JB019075
676 Campbell, M.J., Shaanan, U., Rosenbaum, G., Allen, C.M., Cluzel, D., Maurizot, P., 2018.
677 Permian rifting and isolation of New Caledonia: Evidence from detrital zircon
678 geochronology. Gondwana Research 60, 54–68. https://doi.org/10.1016/j.gr.2018.04.004
679 Cassard, D., Nicolas, A., Rabinovitch, M., Moutte, J., Leblanc, M., Prinzhofer, A., 1981.
680 Structural classification of chromite pods in southern New Caledonia. Economic
681 Geology 76, 805–831.
682 Chew, D.M., Petrus, J.A., Kamber, B.S., 2014. U-Pb LA-ICPMS dating using accessory
683 mineral standards with variable common Pb. Chemical Geology 363, 185–199.
684 https://doi.org/10.1016/j.chemgeo.2013.11.006
685 Cluzel, D., Adams, C.J., Maurizot, P., Meffre, S., 2011. Detrital zircon records of Late

686 Cretaceous syn-rift sedimentary sequences of New Caledonia: An Australian provenance
687 questioned. Tectonophysics 501, 17–27. https://doi.org/10.1016/j.tecto.2011.01.007
688 Cluzel, D., Aitchison, J.C., Picard, C., 2001. Tectonic accretion and underplating mafic
689 terranes in the late Eocene intraoceanic fore-arc of New Caledonia (Southwest Pacific):
690 Geodynamic implications. Tectonophysics 340, 23–59. https://doi.org/10.1016/S0040-
691 1951(01)00148-2
692 Cluzel, D., Aitchison, J.C., Zhou, R., Ireland, T., Heizler, M., Patias, D., Lesimple, S.,
693 Maurizot, P., Teyssier, C., 2022. Direct dating of podiform chromitite: U-Pb (zircon,
694 rutile) and $^{40}Ar/^{39}Ar$ (pargasite) evidence from Tiébaghi Cr deposit (New Caledonia).
695 Ore Geology Reviews 145, 104873. https://doi.org/10.1016/j.oregeorev.2022.104873
696 Cluzel, D., Jourdan, F., Meffre, S., Maurizot, P., Lesimple, S., 2012a. The metamorphic sole
697 of New Caledonia ophiolite: 40Ar/ 39Ar, U-Pb, and geochemical evidence for
698 subduction inception at a spreading ridge. Tectonics 31, 1–18.
699 https://doi.org/10.1029/2011TC003085
700 Cluzel, D., Maurizot, P., Collot, J., Sevin, B., 2012b. An outline of the geology of New
701 Caledonia; from Permian-Mesozoic Southeast Gondwanaland active margin to Cenozoic
702 obduction and supergene evolution. Episodes 35, 72–86.
703 https://doi.org/10.18814/epiiugs/2012/v35i1/007
704 Cluzel, D., Meffre, S., 2002. L'unité de la Boghen (Nouvelle-Calédonie, Pacifique sud-
705 ouest): Un complexe d'accrétion jurassique. Données radiochronologiques préliminaires
706 U-Pb sur les zircons détritiques. Comptes Rendus - Geoscience 334, 867–874.
707 https://doi.org/10.1016/S1631-0713(02)01823-0
708 Cluzel, D., Meffre, S., Maurizot, P., Crawford, A.J., 2006. Earliest Eocene (53 Ma)
709 convergence in the Southwest Pacific: Evidence from pre-obduction dikes in the
710 ophiolite of New Caledonia. Terra Nova 18, 395–402. https://doi.org/10.1111/j.1365-
711 3121.2006.00704.x
712 Cluzel, D., Ulrich, M., Jourdan, F., Meffre, S., Paquette, J.L., Audet, M.A., Secchiari, A.,
713 Maurizot, P., 2016. Early Eocene clinoenstatite boninite and boninite-series dikes of the
714 ophiolite of New Caledonia; a witness of slab-derived enrichment of the mantle wedge
715 in a nascent volcanic arc. Lithos 260, 429–442.
716 https://doi.org/10.1016/j.lithos.2016.04.031
717 Cluzel, D., Whitten, M., Meffre, S., Aitchison, J.C., Maurizot, P., 2018. A Reappraisal of the
718 Poya terrane (New Caledonia): Accreted Late Cretaceous-Paleocene marginal basin
719 upper crust, passive margin sediments, and Early Eocene E-MORB sill complex.

720 Tectonics 37, 48–70. https://doi.org/10.1002/2017TC004579
721 Collot, J., Patriat, M., Sutherland, R., Williams, S., Cluzel, D., Seton, M., Pelletier, B., Roest,
722 W.R., Etienne, S., Bordenave, A., Maurizot, P., 2020. Geodynamics of the SW pacific: A
723 brief review and relations with New Caledonian geology. Geological Society Memoir
724 51, 13–26. https://doi.org/10.1144/M51-2018-5
725 Collot, J.Y., Malahoff, A., Recy, J., Latham, G., Missegue, F., 1987. Overthrust emplacement
726 of New Caledonia ophiolite: Geophysical evidence. Tectonics 6, 215–232.
727 https://doi.org/10.1029/TC006i003p00215
728 Dilek, Y., Furnes, H., 2011. Ophiolite genesis and global tectonics: Geochemical and tectonic
729 fingerprinting of ancient oceanic lithosphere. Bulletin of the Geological Society of
730 America 123, 387–411. https://doi.org/10.1130/B30446.1
731 Gerya, T. V., 2011. Intra-oceanic Subduction Zones. Arc-Continent Collision. 23–51.
732 https://doi.org/10.1007/978-3-540-88558-0_2
733 Gerya, T. V., Stöckhert, B., Perchuk, A.L., 2002. Exhumation of high-pressure metamorphic
734 rocks in a subduction channel: A numerical simulation. Tectonics 21, 1–19.
735 https://doi.org/10.1029/2002tc001406
736 Glen, R.A., 2005. The Tasmanides of eastern Australia. Geological Society Special
737 Publication 246, 23–96. https://doi.org/10.1144/GSL.SP.2005.246.01.02
738 González-Jiménez, J.M., Marchesi, C., Griffin, W.L., Gervilla, F., Belousova, E.A., Garrido,
739 C.J., Romero, R., Talavera, C., Leisen, M., O'Reilly, S.Y., Barra, F., Martin, L., 2017.
740 Zircon recycling and crystallization during formation of chromite- and Ni-arsenide ores
741 in the subcontinental lithospheric mantle (Serranía de Ronda, Spain). Ore Geology
742 Reviews 90, 193–209. https://doi.org/10.1016/j.oregeorev.2017.02.012
743 Grimes, C.B., Wooden, J.L., Cheadle, M.J., John, B.E., 2015. "Fingerprinting" tectono-
744 magmatic provenance using trace elements in igneous zircon. Contributions to
745 Mineralogy and Petrology 170, 1–26. https://doi.org/10.1007/s00410-015-1199-3
746 Kemp, A.I.S., Hawkesworth, C.J., Collins, W.J., Gray, C.M., Blevin, P.L., 2009. Isotopic
747 evidence for rapid continental growth in an extensional accretionary orogen: The
748 Tasmanides, eastern Australia. Earth and Planetary Science Letters 284, 455–466.
749 https://doi.org/10.1016/j.epsl.2009.05.011
750 Liu, C.Z., Xu, Y., Wu, F.Y., 2018. Limited recycling of crustal osmium in forearc mantle
751 during slab dehydration. Geology 46, 239–242. https://doi.org/10.1130/G39869.1
752 Maurizot, P., Bordenave, A., Cluzel, D., Collot, J., Etienne, S., 2020a. Late cretaceous to
753 eocene cover of New Caledonia: From rifting to convergence. Geological Society

754 Memoir 51, 53–91. https://doi.org/10.1144/M51-2017-18
755 Maurizot, P., Cluzel, D., Patriat, M., Collot, J., Iseppi, M., Lesimple, S., Secchiari, A., Bosch,
756 D., Montanini, A., Macera, P., Davies, H.L., 2020b. The Eocene subduction–obduction
757 complex of New Caledonia. Geological Society, London, Memoirs 51, 93–130.
758 https://doi.org/10.1144/m51-2018-70
759 Mortimer, N., Campbell, H.J., Tulloch, A.J., King, P.R., Stagpoole, V.M., Wood, R.A.,
760 Rattenbury, M.S., Sutherland, R., Adams, C.J., Collot, J., Seton, M., 2017. Zealandia:
761 Earth's hidden continent. GSA Today 27, 27–35. https://doi.org/10.1130/GSATG321A.1
762 Moutte, J., 1982. Chromite deposits of the Tiebaghi Ultramafic massif, New Caledonia.
763 Economic Geology 77, 576–591. https://doi.org/10.2113/gsecongeo.77.3.576
764 Murray, C.G., Fergusson, C.L., Flood, P.G., Whitaker, W.G., Korsch, R.J., 1987. Plate
765 tectonic model for the carboniferous evolution of the New England Fold Belt. Australian
766 Journal of Earth Sciences 34, 213–236. https://doi.org/10.1080/08120098708729406
767 Paris, J.P., 1981. Geologie de la Nouvelle-Caledonie: Bureau des Recherches Geologiques et
768 Minieres Memoire. 279 p.
769 Parkinson, I.J., Pearce, J.A., 1998. Peridotites from the Izu-Bonin-Mariana forearc (ODP Leg
770 125): evidence for mantle melting and melt-mantle interaction in a supra-subduction
771 zone setting. Journal of Petrology 39, 1577–1618.
772 https://doi.org/10.1093/petroj/39.9.1577
773 Parrot, J.F., Dugas, F., 1980. The disrupted ophiolitic belt of the southwest Pacific: Evidence
774 of an Eocene subduction zone. Test Tectonophysics 66, 349–372.
775 https://doi.org/10.1016/0040-1951(80)90249-8
776 Paton, C., Hellstrom, J., Paul, B., Woodhead, J., Hergt, J., 2011. Iolite: Freeware for the
777 visualisation and processing of mass spectrometric data. Journal of Analytical Atomic
778 Spectrometry 26, 2508–2518. https://doi.org/10.1039/c1ja10172b
779 Pearce, J.A., Lippard, S.J., Roberts, S., 1984. Characteristics and tectonic significance of
780 supra-subduction zone ophiolites. Geological Society Special Publication 16, 77–94.
781 https://doi.org/10.1144/GSL.SP.1984.016.01.06
782 Pirard, C., Hermann, J., O'neill, H.S.C., 2013. Petrology and geochemistry of the crust-
783 mantle boundary in a Nascent Arc, Massif du Sud Ophiolite, New Caledonia, SW
784 Pacific. Journal of Petrology 54, 1759–1792. https://doi.org/10.1093/petrology/egt030
785 Pujol-Solà, N., Proenza, J.A., Garcia-Casco, A., González-Jiménez, J.M., Román-Alpiste,
786 M.J., Garrido, C.J., Melgarejo, J.C., Gervilla, F., Llovet, X., 2020. Fe-Ti-Zr
787 metasomatism in the oceanic mantle due to extreme differentiation of tholeiitic melts

(Moa-Baracoa ophiolite, Cuba). Lithos 358–359, 105420. https://doi.org/10.1016/j.lithos.2020.105420

Reagan, M.K., Ishizuka, O., Stern, R.J., Kelley, K.A., Ohara, Y., Blichert-Toft, J., Bloomer, S.H., Cash, J., Fryer, P., Hanan, B.B., Hickey-Vargas, R., Ishii, T., Kimura, J.I., Peate, D.W., Rowe, M.C., Woods, M., 2010. Fore-arc basalts and subduction initiation in the Izu-Bonin-Mariana system. Geochemistry, Geophysics, Geosystems 11, 1–17. https://doi.org/10.1029/2009GC002871

Rosenbaum, G., Slade, A., Hoy, D., Rosenbaum, G., 2020. Sedimentological responses to the Hunter – Bowen Orogeny (eastern Australia): evidence from the northern Gympie Terrane Sedimentological responses to the Hunter – Bowen Orogeny (eastern. Australian Journal of Earth Sciences 67, 59–73. https://doi.org/10.1080/08120099.2019.1648317

Sciuba, M., Beaudoin, G., 2021. Texture and trace element composition of rutile in orogenic gold deposits. Economic Geology 116, 1865–1892. https://doi.org/10.5382/ECONGEO.4857

Secchiari, A., Gleissner, P., Li, C., Goncharov, A., Milke, R., Becker, H., Bosch, D., Montanini, A., 2020a. Highly siderophile and chalcophile element behaviour in abyssal-type and supra-subduction zone mantle: New insights from the New Caledonia ophiolite. Lithos 354–355, 105338. https://doi.org/10.1016/j.lithos.2019.105338

Secchiari, A., Montanini, A., Bosch, D., Macera, P., Cluzel, D., 2020b. Sr, Nd, Pb and trace element systematics of the New Caledonia harzburgites: Tracking source depletion and contamination processes in a SSZ setting. Geoscience Frontiers 11, 37–55. https://doi.org/10.1016/j.gsf.2019.04.004

Secchiari, A., Montanini, A., Bosch, D., Macera, P., Cluzel, D., 2016. Melt extraction and enrichment processes in the New Caledonia lherzolites: Evidence from geochemical and Sr-Nd isotope data. Lithos 260, 28–43. https://doi.org/10.1016/j.lithos.2016.04.030

Secchiari, A., Montanini, A., Cluzel, D., 2022. Temperatures and cooling rates recorded by the New Caledonia ophiolite: implications for cooling mechanisms in young forearc sequences. Geochemistry, Geophysics, Geosystems 1–21. https://doi.org/10.1029/2021gc009859

Shi, G., Li, X., Li, Q., Chen, Z., Deng, J., Liu, Y., Kang, Z., Pang, E., Xu, Y., Jia, X., 2012. Ion Microprobe U-Pb age and Zr-in-Rutile thermometry of rutiles from the daixian rutile deposit in the Hengshan Mountains, Shanxi Province, China. Economic Geology 107, 525–535. https://doi.org/10.2113/econgeo.107.3.525

822 Soret, M., Agard, P., Dubacq, B., Vitale-Brovarone, A., Monié, P., Chauvet, A., Whitechurch,
823 H., Villemant, B., 2016. Strain localization and fluid infiltration in the mantle wedge
824 during subduction initiation: Evidence from the base of the New Caledonia ophiolite.
825 Lithos 244, 1–19. https://doi.org/10.1016/j.lithos.2015.11.022
826 Sun, S.S., McDonough, W.F., 1989. Chemical and isotopic systematics of oceanic basalts:
827 Implications for mantle composition and processes. Geological Society Special
828 Publication 42, 313–345. https://doi.org/10.1144/GSL.SP.1989.042.01.19
829 Syracuse, E.M., van Keken, P.E., Abers, G.A., Suetsugu, D., Bina, C., Inoue, T., Wiens, D.,
830 Jellinek, M., 2010. The global range of subduction zone thermal models. Physics of the
831 Earth and Planetary Interiors 183, 73–90. https://doi.org/10.1016/j.pepi.2010.02.004
832 Tomkins, H.S., Powell, R., Ellis, D.J., 2007. The pressure dependence of the zirconium-in-
833 rutile thermometer. Journal of Metamorphic Geology 25, 703–713.
834 https://doi.org/10.1111/j.1525-1314.2007.00724.x
835 Triebold, S., von Eynatten, H., Zack, T., 2012. A recipe for the use of rutile in sedimentary
836 provenance analysis. Sedimentary Geology 282, 268–275.
837 https://doi.org/10.1016/j.sedgeo.2012.09.008
838 Ulrich, M., Picard, C., Guillot, S., Chauvel, C., Cluzel, D., Meffre, S., 2010. Multiple melting
839 stages and refertilization as indicators for ridge to subduction formation: The New
840 Caledonia ophiolite. Lithos 115, 223–236. https://doi.org/10.1016/j.lithos.2009.12.011
841 Vermeesch, P., 2018. IsoplotR: A free and open toolbox for geochronology. Geoscience
842 Frontiers 9, 1479–1493. https://doi.org/10.1016/j.gsf.2018.04.001
843 Vermeesch, P., 2012. On the visualisation of detrital age distributions. Chemical Geology
844 312–313, 190–194. https://doi.org/10.1016/j.chemgeo.2012.04.021
845 Wiedenbeck, M., Alle, P., Corfu, F., Grififn, W.L., Meier, M., Oberli, F., Quadt, A. V.,
846 Roddick, J.C., Spiegel, W., 1995. Three natural zircon standards for U□Th□Pb, Lu□Hf,
847 trace element and REE analyses. Geostandards Newsletter 19, 1–23.
848 https://doi.org/10.1111/j.1751-908X.1995.tb00147.x
849 Yamamoto, S., Komiya, T., Yamamoto, H., Kaneko, Y., Terabayashi, M., Katayama, I.,
850 Iizuka, T., Maruyama, S., Yang, J., Kon, Y., Hirata, T., 2013. Recycled crustal zircons
851 from podiform chromitites in the Luobusa ophiolite, southern Tibet. Island Arc 22, 89–
852 103. https://doi.org/10.1111/iar.12011
853 Yu, M., Dilek, Y., Yumul, G.P., Yan, Y., Dimalanta, C.B., Huang, C.Y., 2020. Slab-controlled
854 elemental–isotopic enrichments during subduction initiation magmatism and variations
855 in forearc chemostratigraphy. Earth and Planetary Science Letters 538, 116217.

https://doi.org/10.1016/j.epsl.2020.116217

Zack, T., Stockli, D.F., Luvizotto, G.L., Barth, M.G., Belousova, E., Wolfe, M.R., Hinton, R.W., 2011. In situ U-Pb rutile dating by LA-ICP-MS: ^{208}Pb correction and prospects for geological applications. Contributions to Mineralogy and Petrology 162, 515–530. https://doi.org/10.1007/s00410-011-0609-4

862 **Appendices**

863

864 *Appendix A*: Samples location, mineral characteristics and imaging, detailed analytical
865 procedures and Dark-grey rutile U-Pb dating plots.

866

867 This appendix provides extra information that support the manuscript, including: (i)
868 Geological map and schematic stratigraphic column of the study area; (ii) mineral processing
869 workflow; (iii) Raman spectra of studied TiO_2 polymorphs; (iv) tables detailing zircon and
870 TiO_2 polymorphs characteristics (v) CL and SEM images, and EDX mapping of minerals of
871 interest; (v) Zircon and TiO_2 polymorphs U-Pb dating and trace element analysis data
872 processing and validation.

873

874 *Appendix B*: Excel spreadsheet containing Zircon and TiO_2 polymorphs U-Pb and trace
875 element isotopes data.

876

877

Figure 1 (high-resolution) Click here to access/download;Figure;01_Map New caledonia_Patias version-01.tif

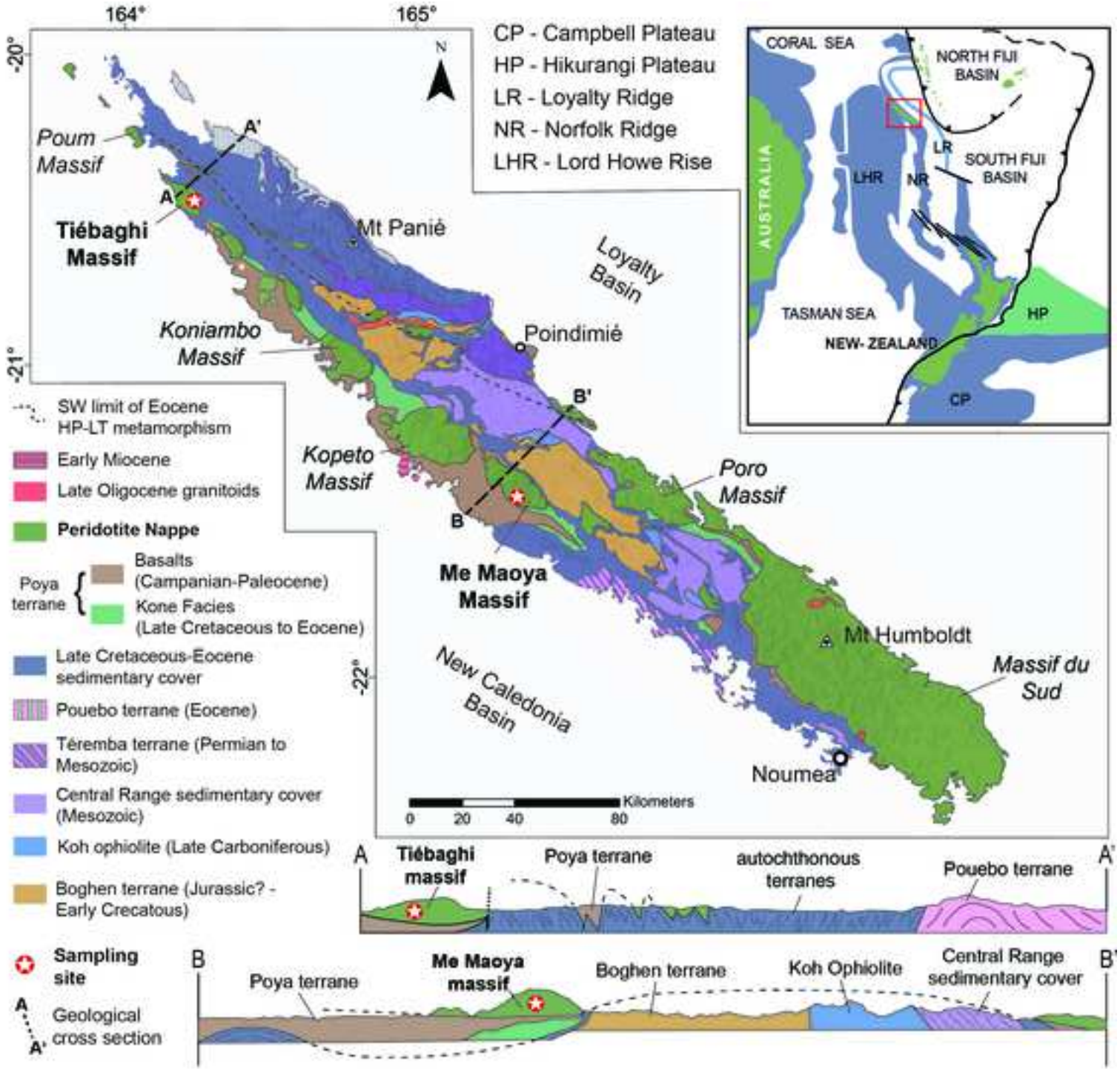

Figure 2 (high-resolution)

Click here to access/download;Figure;02_Patias_Samples-03.jpg

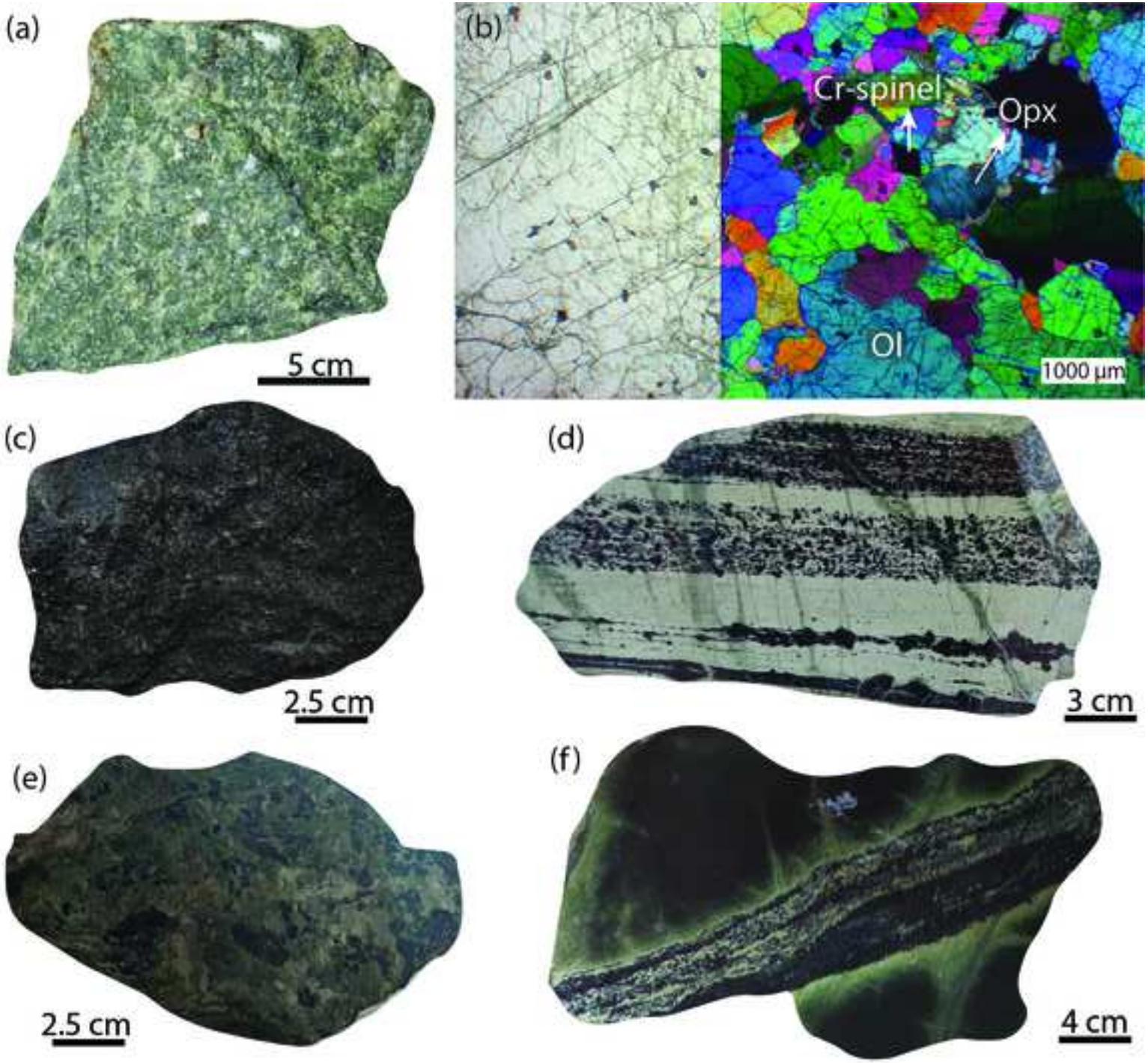

Figure 3 (high-resolution)

Click here to access/download;Figure;03_Patias_Rut and zirc-03-03.jpg

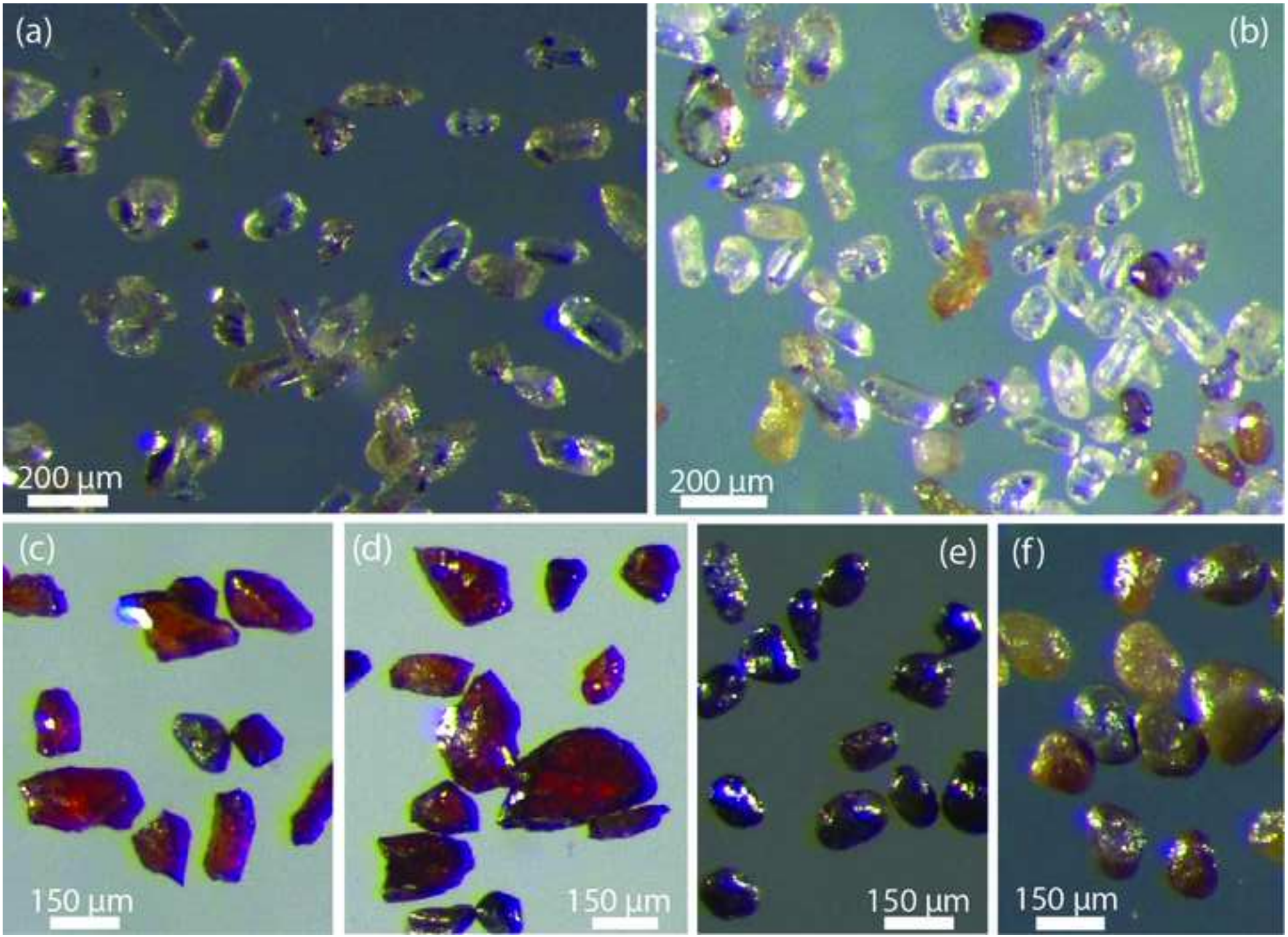

Figure 4 (high-resolution)

Click here to access/download;Figure;04_Patias_Zircons NC_Ages.tif

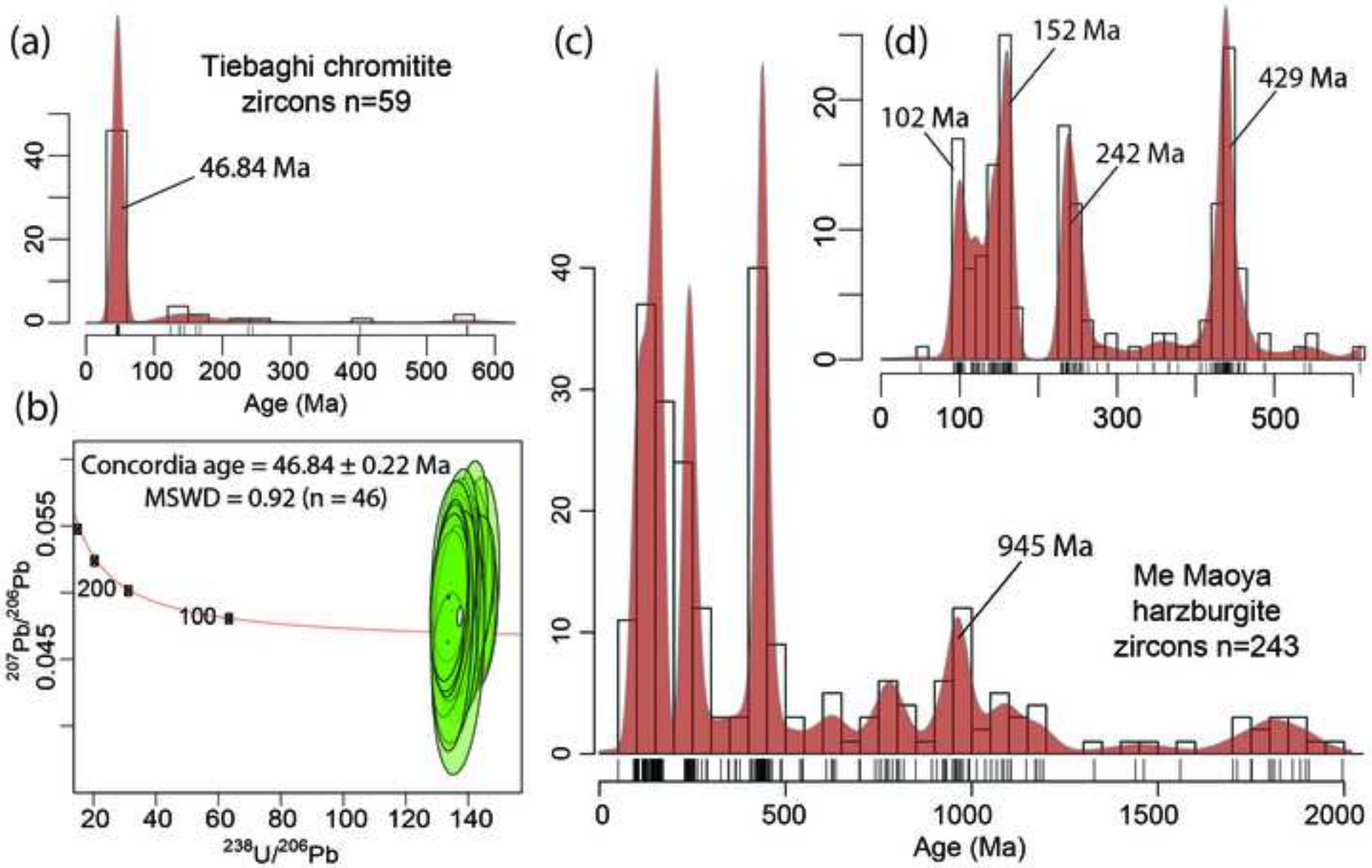

Figure 5 (high-resolution)

Click here to access/download;Figure;05_Patias_Trace zircons.jpg

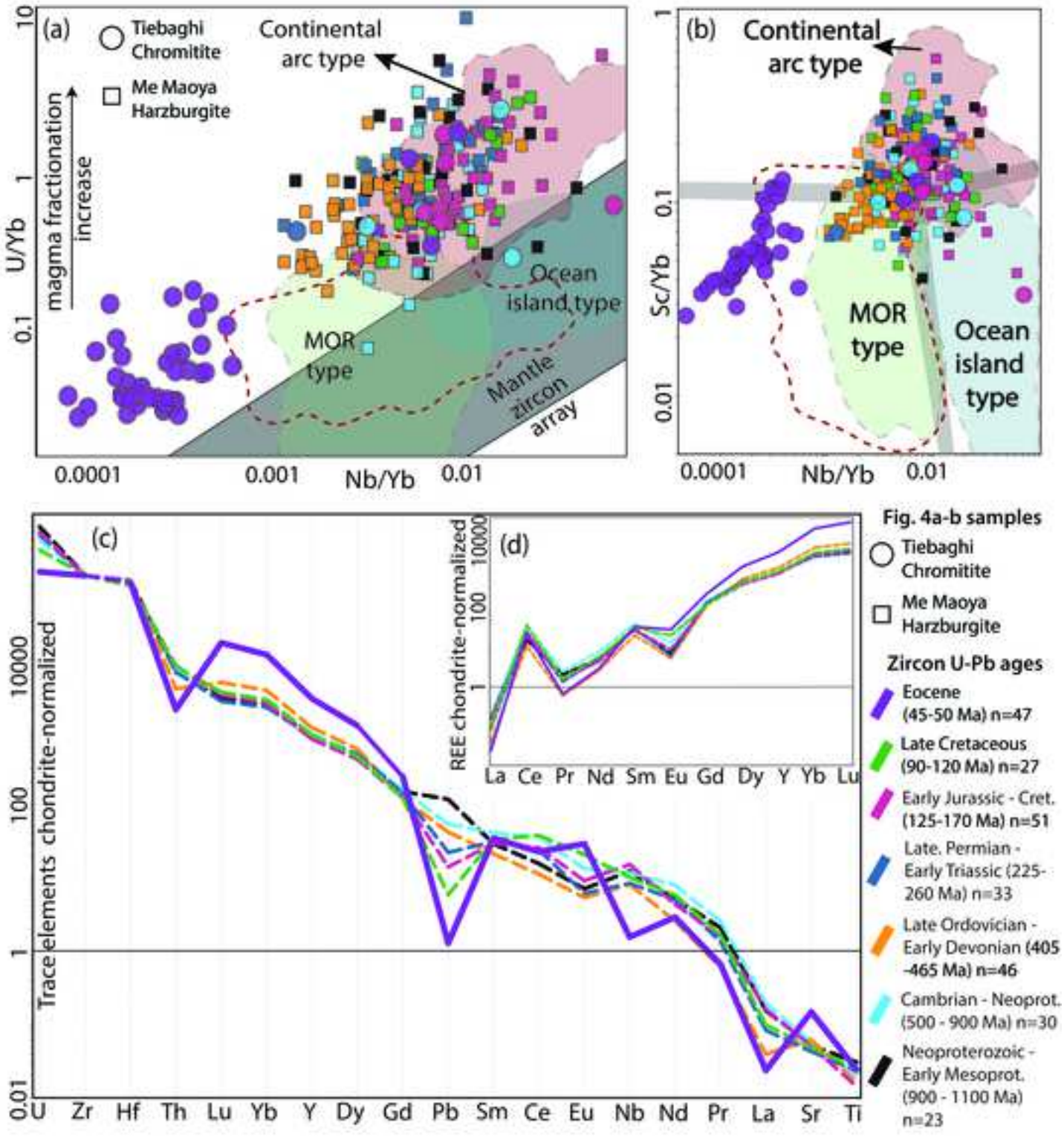

Figure 6 (high-resolution)

Click here to access/download;Figure;06_Patias_Rutiles ages-02.jpg

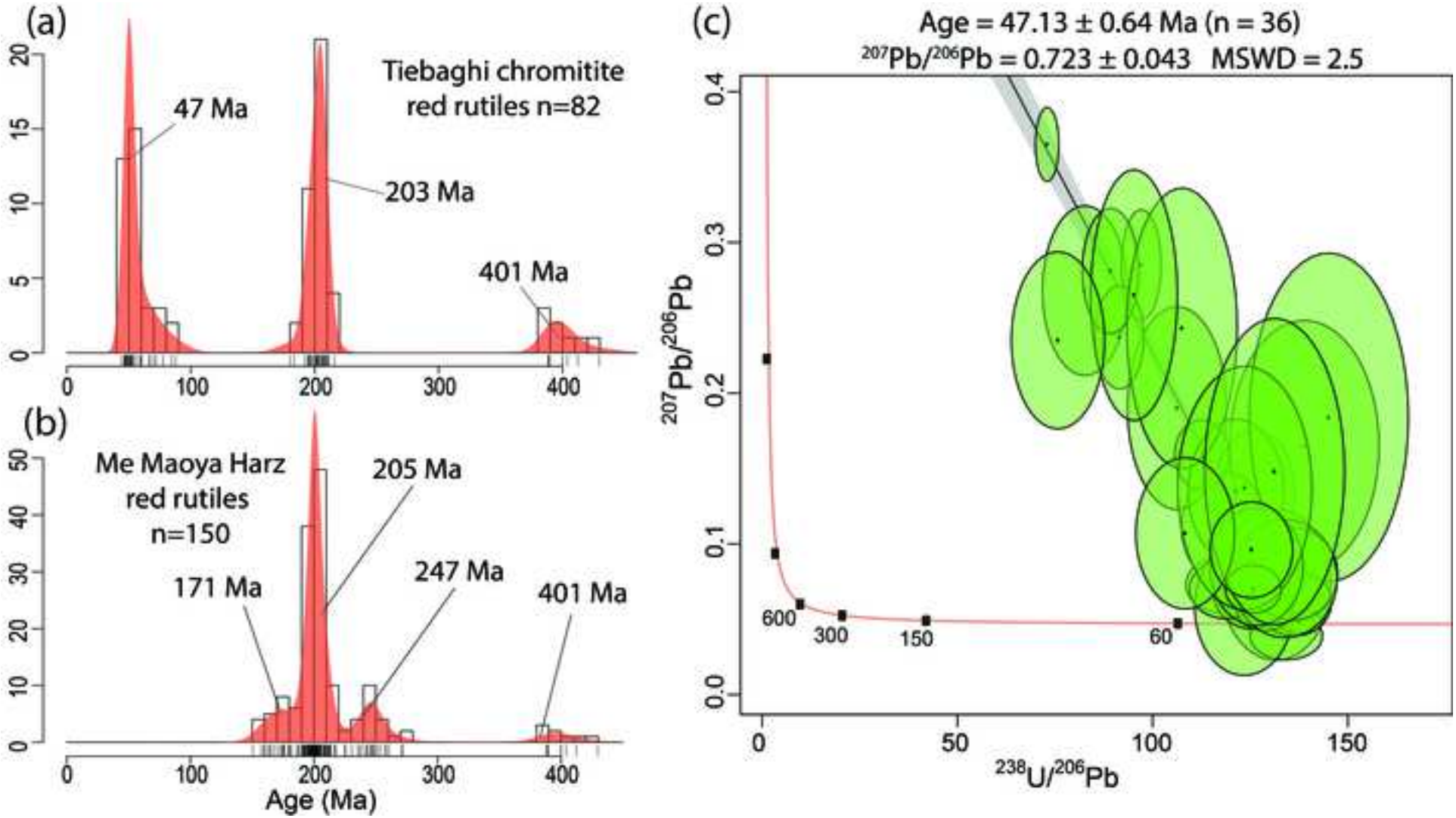

Figure 7 (high-resolution)

Click here to access/download;Figure;07_Patias_Trace elements rutiles plots-01-01-01-01.jpg

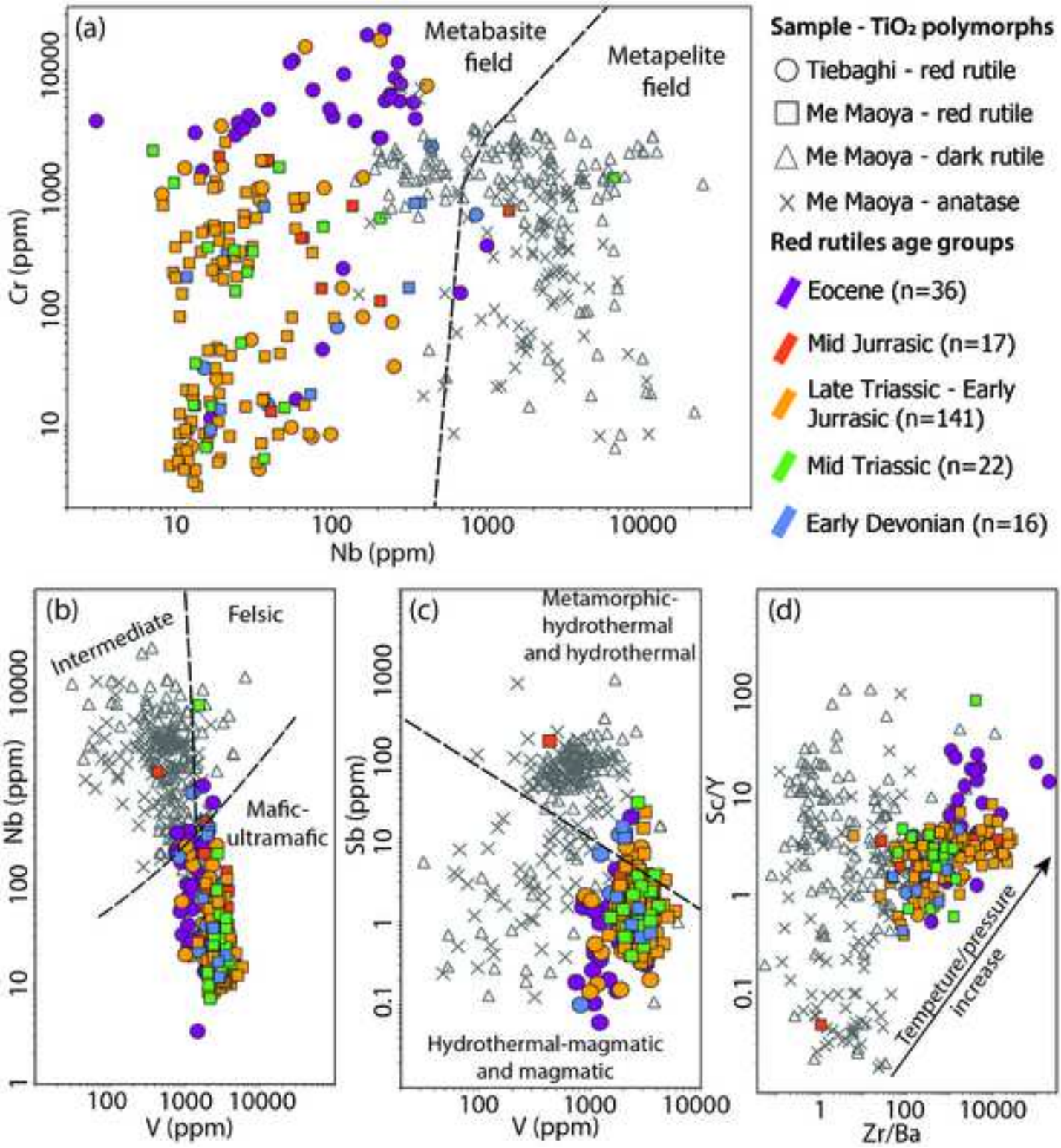

Figure 8 (high-resolution)

Click here to access/download;Figure;08_Patias_Trace elements rutiles plots-01-02.jpg

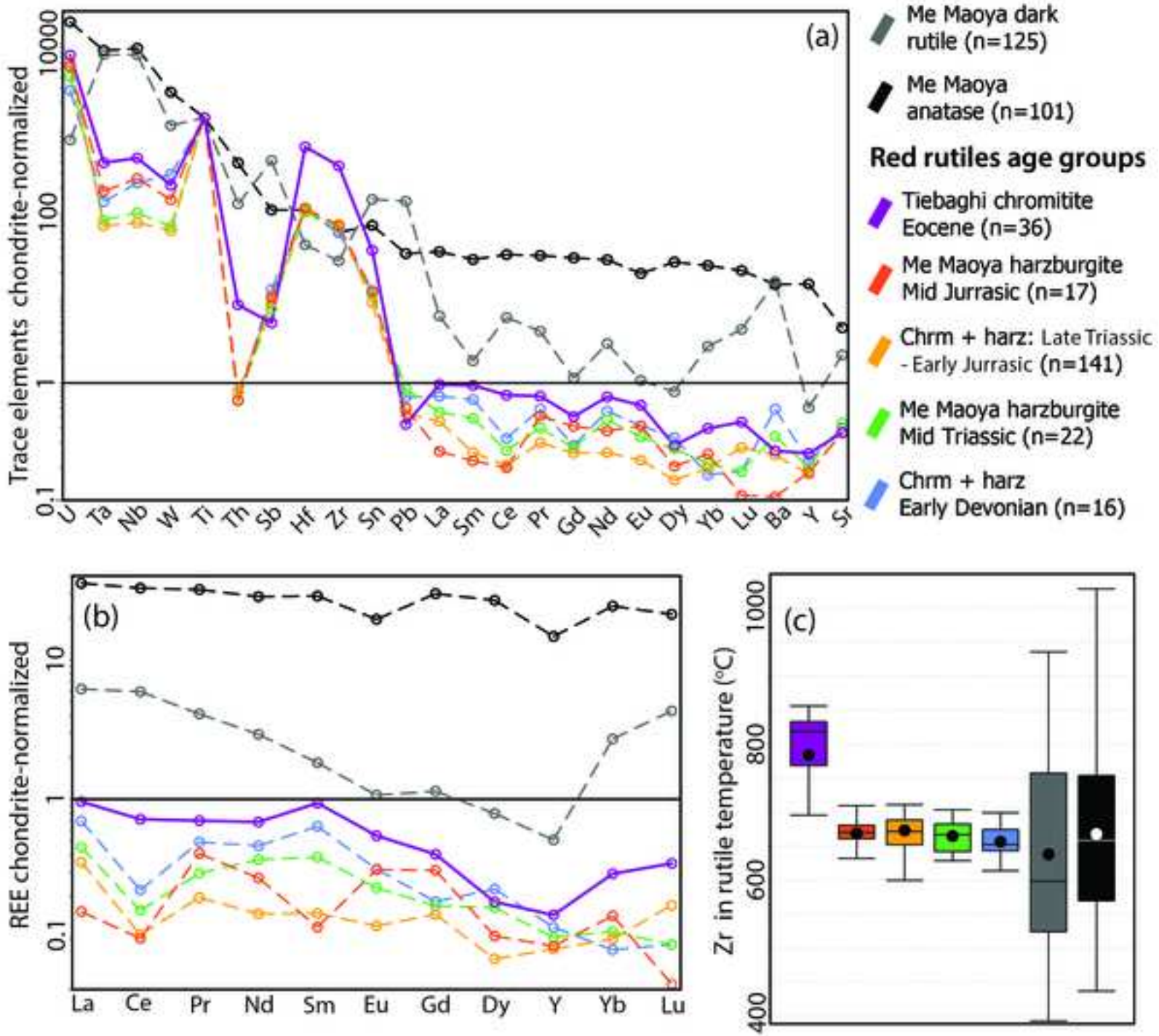

Figure 9 (high-resolution)

Click here to access/download;Figure;09_Zircons and rutiles KDE discussion_V3_teste-01.jpg

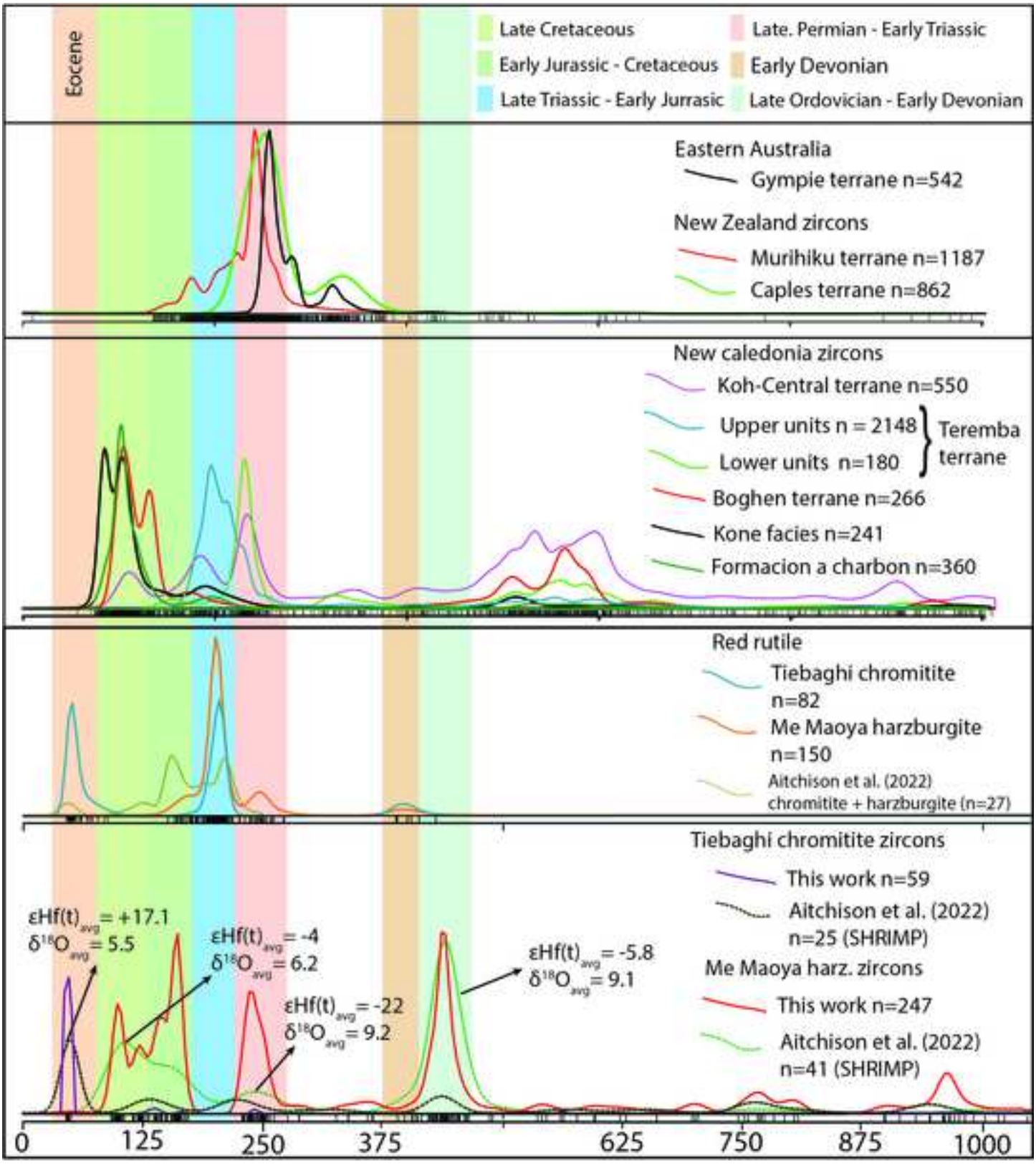

Figure 10 (high-resolution)

Click here to access/download;Figure;10_Patias_Subduction recycling process-01-01.jpg

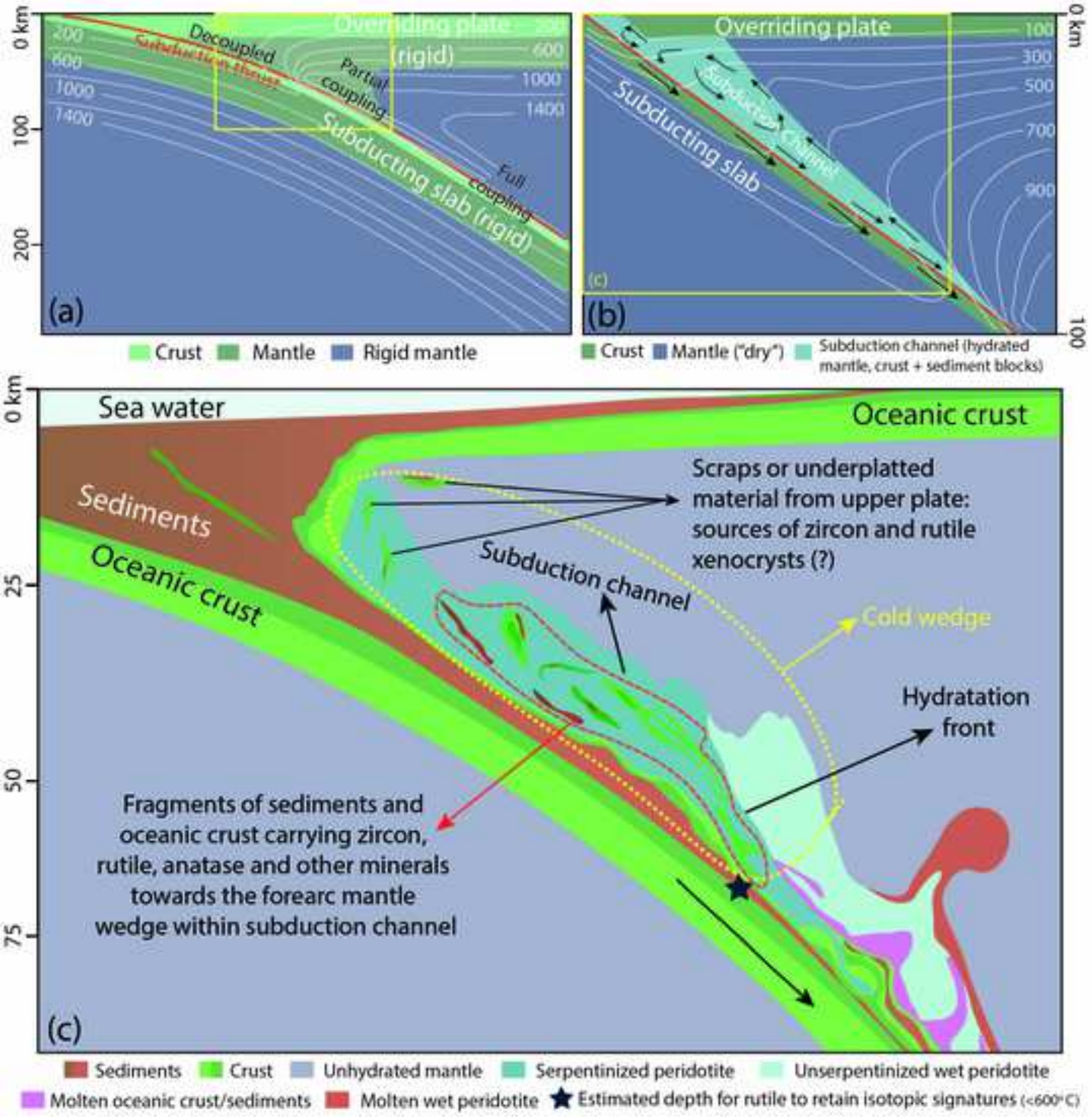

Supplementary material for online publication only

Click here to access/download
Supplementary file
04_Patias_Appendix A.docx

Supplementary material for online publication only

Click here to access/download
Supplementary file
05_Patias_Appendix B.xlsx

Declaration of interests

☒ The authors declare that they have no known competing financial interests or personal relationships that could have appeared to influence the work reported in this paper.

☐The authors declare the following financial interests/personal relationships which may be considered as potential competing interests: